ORIGINAL ARTICLE

Journal Section

Dynamics of diabatically forced anticyclonic plumes in the stratosphere

Aurélien Podglajen[1] | Bernard Legras[1] | Guillaume Lapeyre[1] | Riwal Plougonven[1] | Vladimir Zeitlin[1] | Vincent Brémaud[1] | Pasquale Sellitto[2,3]

[1]LMD/IPSL, École Polytechnique, Institut Polytechnique de Paris, ENS, PSL Université, Sorbonne Université, CNRS, Palaiseau France

[2]Univ. Paris Est Créteil and Université de Paris Cité, CNRS, Laboratoire Interuniversitaire des Systèmes Atmosphériques (LISA-IPSL), Institut Pierre-Simon Laplace, Créteil, France

[3]Istituto Nazionale di Geofisica e Vulcanologia, Osservatorio Etneo, Catania, Italy

Correspondence
Aurélien Podglajen, Laboratoire de Météorologie Dynamique (LMD), École Polytechnique, Palaiseau, 91128, France
Email: aurelien.podglajen@lmd.ipsl.fr

Funding information

A new class of vortices has been observed in the stratosphere following extreme wildfires (Canada 2017, Australia 2020) and volcanic eruptions (Raikoke 2019). These vortices are long-lived mesoscale anticyclones (100s to 1000 km in diameter) trapping plumes of aerosols and combustion/volcanic compounds. Due to their unusual composition, these anticyclonically trapped plumes (ATPs) are associated with a significant radiative heating which fuels their ascent through the stratosphere. The present paper investigates the dynamics of ATPs using two complementary approaches: analytically, in a potential vorticity (PV) perspective, and through idealized numerical simulations with the Weather Research and Forecast (WRF) model. In both cases, we consider the vortical flow forced by a heating Lagrangian tracer. By reformulating the problem in the potential radius-potential temperature coordinate system introduced for tropical cyclones, we first clarify that ATP formation is concomitant with the injection of air into the stratified flow at extratropical latitudes. Then, we derive a set of simplified 1-dimensional equations describing the subsequent evolution of the inviscid flow. The equation obtained for the tracer is a variant of the classical Burgers' equation. In qualitative agreement with the 3D WRF simulations, this the-

oretical model predicts that ATPs evolve into asymmetrical structures with an upper tracer front associated with sustained near-zero anticyclonic PV, followed by a smooth tracer tail where cyclonic PV develops. Radiative relaxation of the temperature perturbations induced by the anticyclone and the presence of an initial PV anomaly tend to stabilize ATPs during their ascent. Finally, we note that the theory predicts a similar relationship between the plume and anticyclonic PV for cooled ATPs, which is supported by 3D simulations and may apply to the 2022 Hunga Tonga-Hunga Ha'apai volcanic plume.

KEYWORDS
wildfire plume, volcanic plume, potential vorticity, diabatic heating, geophysical fluid dynamics, stratosphere

1 | INTRODUCTION

While the flow in the mid-latitude lower stratosphere is generally characterised by slow diabatic vertical transport (Brewer, 1949; Butchart, 2014), extreme events such as intense pyroconvection from wildfires (Fromm et al., 2010) or large volcanic eruptions (Holasek et al., 1996; Carr et al., 2022) can result in a rapid and direct injection, into the stratosphere, of air from lower levels charged with combustion products or volcanogenic compounds. Such injections have the ability to alter stratospheric composition and general circulation for years (e.g. Brown et al., 2023). They also have significant impacts on the global radiative budget (Schallock et al., 2023).

For a few years, it has been recognised that stratospheric plumes may feature specific mesoscale dynamics. A typical example is the plume from the 2019-2020 Australian wildfires, which self-organised into several long-lived coherent smoke patches. These ellipsoidal smoke 'bubbles', which are typically a few kilometers deep and hundreds of kilometers wide, ascended through the mid-latitude stratosphere while maintaining a compact structure (Khaykin et al., 2020; Kablick et al., 2020; Pumphrey et al., 2021). Atmospheric reanalyses have revealed that the persistence of those structures despite stirring by the large-scale flow resulted from the confinement of the plume within anticyclonic vortices. The largest of those anticyclonically trapped plume (ATP) bubbles was associated with a 1000-km diameter vortex, and remained visible as an ascending isolated patch of ash for 3 months, rising from 16 to 36 km. Since then, similar smoke anticyclones have been identified retrospectively in the aftermath of the 2017 wildfires in British Columbia (Lestrelin et al., 2021). In both cases, diabatic lofting of the smoke plume, reaching several degrees of potential temperature per day (e.g., Boers et al., 2010; de Laat et al., 2012; Khaykin et al., 2018; Yu et al., 2019; Khaykin et al., 2020), was attributed to the absorption of solar radiation by black carbon aerosols. A similar phenomenon may have taken place in the ash-rich aerosol cloud from the 2019 eruption of the Raikoke volcano (Khaykin et al., 2022b), which coalesced into horizontally circular patches (Cai et al., 2022) and ascended from 18 to 25 km in the course of a few months (Chouza et al., 2020).

More recently, the eruption of the Hunga Tonga-Hunga Ha'apai volcano generated the largest and highest stratospheric injection since at least the eruption of Mount Pinatubo in 1991, with the main detrainment located around

35 km altitude (e.g., Carr et al., 2022; Proud et al., 2022; Khaykin et al., 2022a). This time, the plume consisted of sulphur compounds and water vapour (Millán et al., 2022; Khaykin et al., 2022a), and the latter generated substantial in-plume diabatic cooling and a rapid descent (Sellitto et al., 2022). Although this feature was not captured by the ECMWF operational analyses, Legras et al. (2022) noted using a suite of spaceborne instruments that the plume tended to roll-up and was associated with a wind anomaly consistent with an anticyclonic vorticity anomaly. This anticyclonic rotation lasted over a few weeks following the eruption.

The role of vorticity anomalies in isolating air masses and preserving them from dilution within the environment is well-understood in the case of *adiabatic* geophysical flows (e.g., Schoeberl et al., 1992; Garny and Randel, 2013). However, the coupling between the dynamics and diabatic forcing *within* a stratospheric plume has received less attention. Consequently, the processes responsible for the formation and maintenance of ATPs remain unclear in the literature. Doglioni et al. (2022) simulated smoke-charged vortices in the GEOSCCM global model by introducing sunlight-absorbing aerosols, but did not investigate the mechanisms behind the observed dynamics of the plume. Lestrelin et al. (2021) carefully analysed the structure of Australian and Canadian smoke vortices in CALIOP spaceborne lidar observations and the ERA5 reanalysis. They found that the ellipsoidal anticyclone-trapped smoke plumes had a vertical-to-horizontal aspect ratio of the order of f/N where f and N are the Coriolis and Brunt-Väisälä frequencies. Interestingly, at the center of the anomaly, ERA5 indicated near-zero absolute vorticity and potential vorticity (PV).

Lestrelin et al. (2021) proposed to interpret low absolute-PV smoke anticyclones as resulting from the vertical transport of a smoke-charged tropospheric air mass, conserving both its low PV and its tropospheric composition during its diabatic ascent through the stratosphere. This conjecture was used by Khaykin et al. (2022b) to explain the confinement and anticyclonic motion of the Raikoke volcanic plume. Nevertheless, this theory is incomplete from a dynamical point of view: by considering Lagrangian conservation of PV, it overlooks the contribution of diabatic heating to its evolution (e.g. Hoskins et al., 1985; Haynes and McIntyre, 1987).

The goal of the present paper is to investigate the dynamics governing the formation and maintenance of cooled and heated ATPs and in particular their connection with the dynamics of potential vorticity. We propose a conceptual model based on theoretical considerations and confront it with observations and numerical simulations. The article is organised as follows. In Section 2, we revisit the observational evidence for plume vortices and highlight particular properties. In Section 3, we review the theory of potential vorticity dynamics in diabatically forced axisymmetric flows and derive a set of simplified equations describing the joint evolution of potential vorticity and a diabatically active tracer. Section 4 presents results from numerical simulations of a heated tracer plume, and compares them with the theory. Section 5 contains a discussion. Conclusions and recommendations for future work are outlined in Section 6.

2 | OBSERVATIONS OF THE 2020 SMOKE-CHARGED VORTEX KOOBOR

Observations of the 2020 Australian wildfire plume are revisited in order to highlight some special properties of the aerosol cloud and associated vortex which have not been emphasised in previous studies. We use the 532 nm total attenuated backscatter data from the spaceborne lidar CALIOP (Cloud-Aerosol lidar with Orthogonal Polarization) onboard the CALIPSO satellite (Vaughan et al., 2004; Winker et al., 2010), specifically version 4.50 (Kar et al., 2018; Getzewich et al., 2018) of the level 1 product. Global Navigation Satellite System (GNSS) radio-occultation (RO) temperature soundings are obtained from " dry retrievals" from the COSMIC Data Analysis and Archive center (CDAAC) website `https://cdaac-www.cosmic.ucar.edu/`. Other temperature and potential vorticity fields are derived from the ERA5 reanalysis (Hersbach et al., 2020).

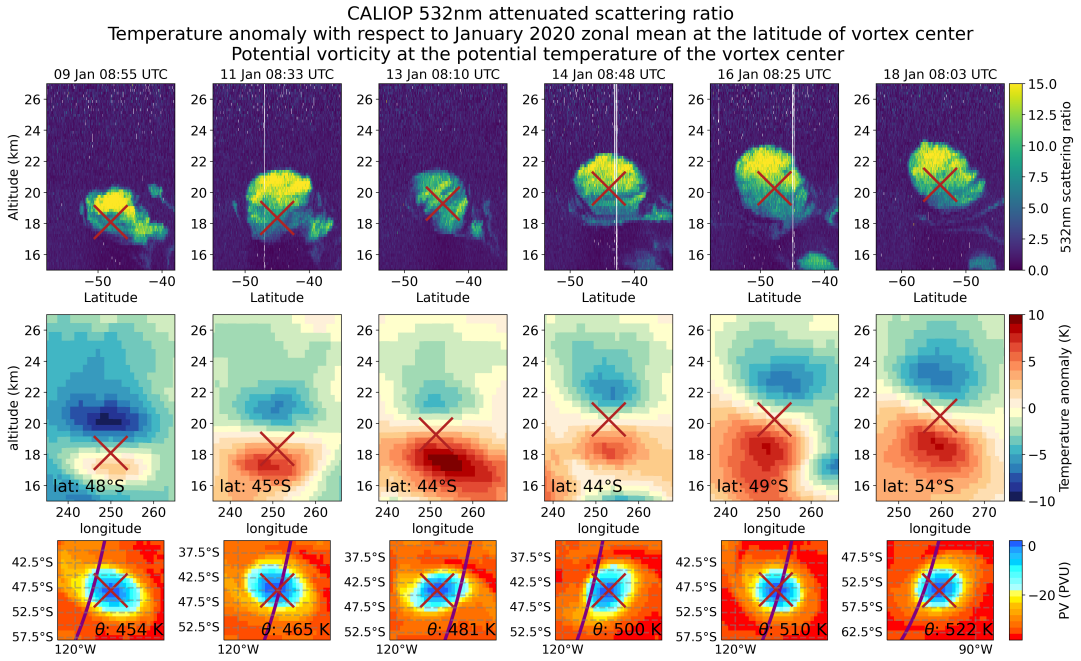

FIGURE 1 Top row: selected sections of CALIOP 532 nm attenuated backscatter ratio. The crosses indicate the altitude and latitude of the associated anticyclone in ERA5. Middle row: corresponding height-longitude sections of ERA5 temperature anomaly at the latitude of the vortex center, defined with respect to the zonal mean. The crosses indicate the altitude and longitude of the vortex center. Bottom row: Horizontal charts of potential vorticity at the potential temperature level of the vortex center (whose horizontal location is shown by the cross). The purple curves represent the track of CALIOP corresponding to the sections in the top row.

CALIOP observations of attenuated backscatter ratio were instrumental in the discovery of stratospheric plume vortices (Khaykin et al., 2020; Kablick et al., 2020). The main vortex, nicknamed Koobor in reference to an aboriginal legend (Lestrelin et al., 2021), could be followed over three months in the stratosphere with the lidar. Figure 1 (top row) displays selected vertical sections of CALIOP backscatter ratio across Koobor between 9 and 16 January 2020, together with (middle row) vertical sections of temperature zonal anomaly and (bottom row) horizontal sections of PV, both from ERA5. The backscatter ratio shown here is the ratio of the measured total attenuated backscatter profile over the theoretical molecular backscatter (Vaughan et al., 2004). It appears artificially reduced within and below thick plumes due to the attenuation of the laser beam.

In agreement with previous studies, CALIOP observations in Figure 1 evidence an ascent of Koobor over time. According to ERA5, the aerosol cloud is accompanied by a temperature anomaly dipole associated with the anticyclonic vortex, with the cold anomaly located above the plume. The latitude-longitude track of CALIPSO's orbit is displayed in the bottom row of Figure 1 and shows a good correspondence between anticyclonic PV in ERA5 and the smoke cloud. During this early phase of its life, Koobor was horizontally stagnating over the Pacific (bottom panels of Figure 1) but ascending rapidly from 19 to 22 km over 9 days.

Besides the ascent of Koobor, we further note that the attenuated backscatter ratio in Figure 1 (top panels) is not uniform within the plume, with larger values found near its top than in its lower part. This vertical gradient could

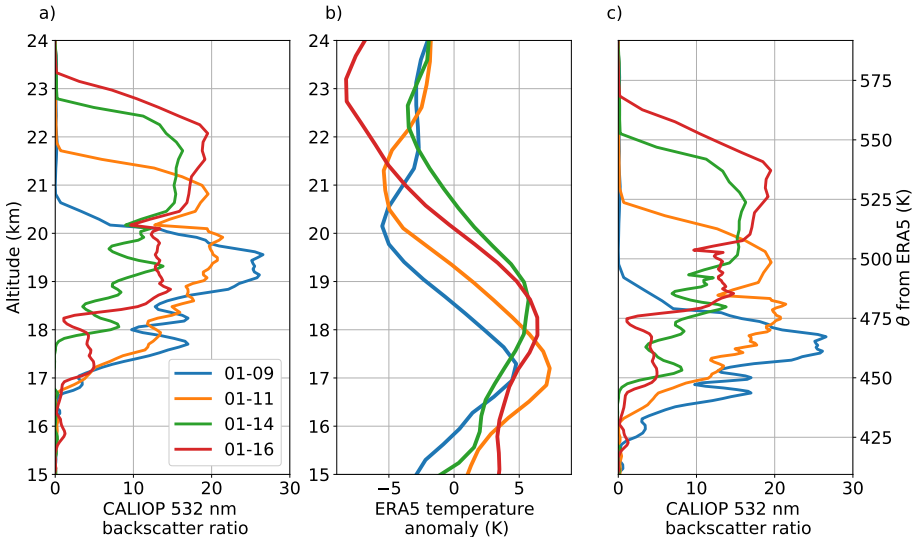

FIGURE 2 (a) Vertical profiles of CALIOP 532 nm (attenuation-corrected) backscatter ratio across Koobor at the latitude of the associated vortex center for 4 night orbits between 9 and 16 January 2020 chosen for the proximity of the CALIOP orbit to the vortex. The full cross-sections of attenuated backscatter ratio and exact times of the orbits are provided in Figure 1. (b) Colocated ERA5 temperature zonal anomaly profiles. (c) Same as panel (a) but with the ERA5 potential temperature as vertical coordinate.

arise from actual variations in aerosol properties, but also from the partial attenuation of CALIOP's laser beam. To disentangle the two contributions, we retrieved profiles of attenuation-corrected backscatter ratio at the center of the smoke plume for a subset of the sections in Figure 1. The lidar ratio (assumed constant) needed for the inversion is constrained for each profile using the attenuation of the molecular backscatter signal in the clear-sky stratosphere below the smoke cloud. The values obtained lie between 50 and 75, on the lower side of the range of lidar ratios reported by Ohneiser et al. (2020) for the 2020 Australian smoke plume.

The resulting profiles of attenuation-corrected backscatter ratio are depicted in Figure 2. They also show vertical variations, thereby demonstrating that the vertical gradients noted in Figure 1 are not solely due to the attenuation of CALIOP's laser beam, but also originate from heterogeneities in aerosol properties. If the optical and microphysical properties of the aerosol particles were homogeneous throughout the plume, this quantity would be directly proportional to the aerosol mixing ratio (in either mass or number). The profiles exhibit an asymmetrical, sawtooth-like pattern, with a sharp front at the top of the cloud and a smoothly sloping (and sometimes perturbed) tail trailing behind. Furthermore, the bottom of the cloud seems to rise more slowly than its top, and the vertical extent of the plume to increase with time.

Figure 2b shows ERA5 temperature zonal anomaly profiles at the location of the backscatter ratio profiles in panel (a). The minimum of the temperature anomaly remains located at the front of the aerosol sawtooth, while the maximum gets broader with time as the aerosol tail develops. In this oceanic area void of radiosonde stations, the ERA5 reanalysis primarily relies on the assimilation of satellite observations of the temperature field. The capacity of the assimilation system to follow the observed temperature profiles is illustrated in Figure 3 for an encounter between Koobor and one of its siblings, denoted as vortex V2, which occurred on 15 January 2020. Koobor originated from an intense event of pyroconvection on 29-31 December 2019, while V2 formed after a similar case on 4 January 2020 (Peterson

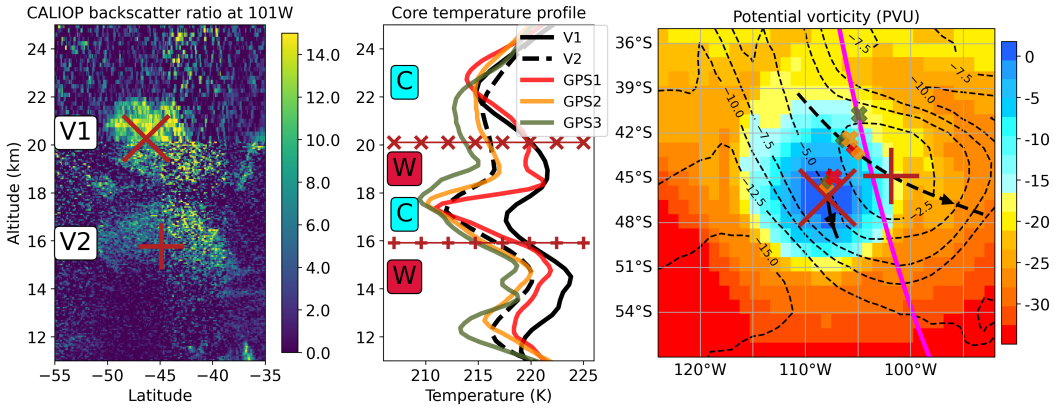

FIGURE 3 (a) Section of CALIOP 532 nm total attenuated backscatter ratio on 15 January 2020 at 21:03 UTC (time J). The two crosses indicate the latitude and altitude of Koobor (K) and the second vortex (V2) at time J in ERA5. (b) Vertical profiles of temperature at the location of the two vortices according to ERA5 (black curves) and to three nearby GPS soundings on 15 January, denoted as GPS1 (KOMPSAT5, 14:29 UTC), GPS2 (COSMIC2, 15:22 UTC) and GPS3 (TSX, 12:32 UTC). The selected profiles are located within 600 km of both vortices. The horizontal lines with crosses indicate the altitude of the two vortices (20.1 km for Koobor, 15.9 km for V2) (c) ERA5 potential vorticity maps of Koobor (colour) and V2 (contours) at the isentropic level of their center (503 K for Koobor, 408 K for V2). The black lines indicate the trajectories of the two vortices in the time interval [J-18h,J+18h]. The large crosses indicate the location of the two vortices at time J. The locations of the GPS-RO soundings are shown as crosses (colours as in (b)) and the locations of the vortices at the time of CALIOP's section are depicted by diamonds. The pink curve represents the track of CALIOP corresponding to the sections in panel (a).

et al., 2021). Figure 3 shows the two clouds in a single cross-section of CALIOP (panel a) and the corresponding track of CALIPSO, which intersects the two vortices (panel c). In Figure 3b, ERA5 temperature profiles at the location of the cores of the two ATPs are compared with 3 nearby GPS radio-occultation (GPS-RO) soundings (their exact location is indicated in panel c). The superposition of two anticyclones is associated with a double temperature dipole, which ERA5 follows with remarkable fidelity. While the reanalysis accurately reproduces the temperature structure of the vortices, other meteorological fields, such as PV, may be less reliable. In particular, ERA5 reconstructs a single-signed, quasi-ellipsoidal PV anomaly matching the size of the aerosol cloud, but neither the exact shape of the vortices nor the distribution of the PV are directly constrained by the assimilated observations. Nevertheless, we note that, over its lifetime, ERA5 consistently indicates a near-zero PV at the center of Koobor (Figure 3c, also see Lestrelin et al. (2021)). This low absolute value of PV is very uncommon in the mid-latitude stratosphere, but we will see in the following sections that it is predicted both by the theory and by the numerical simulations.

3 | THEORY

3.1 | Potential vorticity budget of an axisymmetric flow

Given their typical scales, ATPs in rotating stratified fluids can be studied using tools from potential vorticity theory (Hoskins et al., 1985). As a first approximation, these structures can be considered axisymmetric, an assumption supported by the observations (see Figure 3). Isolated axisymmetric vortices are a long-studied topic in fluid mechanics.

Regarding atmospheric applications, Eliassen (1952) introduced the model of a quasi-stationary axisymmetric vortex, in which the azimuthal wind field is in gradient wind balance with a radial temperature anomaly. This equilibrium state of the flow is sometimes referred to as the Eliassen balanced vortex model (Schubert and Hack, 1983). Eliassen's seminal work was later developed to investigate tropical cyclone dynamics from the point of view of potential vorticity (see, e.g., Schubert, 2018, and references therein). In the following, we will rely on a framework introduced by Schubert and Alworth (1987) and Schubert (2018) for tropical cyclones, adapting it to the case of ATPs.

The starting point is the dynamics of Ertel's potential vorticity (PV) (Ertel, 1942), noted P, which is expressed in Cartesian coordinates as:

$$P = \frac{1}{\rho}\boldsymbol{\zeta_a} \cdot \boldsymbol{\nabla}\theta \tag{1}$$

where ρ is the density, θ the potential temperature and $\boldsymbol{\zeta_a}$ the absolute vorticity vector. In an inviscid (i.e., neglecting non-conservative mechanical forcing) adiabatic flow, PV behaves like an inert tracer and is materially conserved. On the contrary, in the case of vortices subject to diabatic heating or mechanical forcing, Lagrangian conservation of P is no longer guaranteed. In Cartesian coordinates, the PV tendency equation reads (e.g., Andrews et al., 1987):

$$\frac{\mathrm{D}P}{\mathrm{D}t} = \frac{1}{\rho}\boldsymbol{\zeta_a} \cdot \boldsymbol{\nabla}Q + \frac{1}{\rho}\boldsymbol{\nabla}\theta \cdot \boldsymbol{\nabla} \times \mathbf{F} \tag{2}$$

with $Q = \mathrm{D}\theta/\mathrm{D}t = \dot{\theta}$ the diabatic heating rate and $\mathbf{F}$ the mechanical forcing.

In this paper, we restrict ourselves to the case of an axisymmetric flow on the $f-$plane, where f is the Coriolis parameter. With r the radial coordinate, u, v the components of the horizontal wind in the radial and azimuthal directions, respectively, PV may be expressed as (e.g. Shutts, 1991; Schubert, 2018):

$$P = \frac{f}{2\rho\, r}\left|\frac{\partial(R^2,\theta)}{\partial(r,z)}\right| = \frac{f}{2\rho\, r}\left(\frac{\partial R^2}{\partial r}\frac{\partial \theta}{\partial z} - \frac{\partial R^2}{\partial z}\frac{\partial \theta}{\partial r}\right) \tag{3}$$

where we use the notation $\left|\frac{\partial(a,b)}{\partial(x,y)}\right| = \frac{\partial a}{\partial x}\frac{\partial b}{\partial y} - \frac{\partial a}{\partial y}\frac{\partial b}{\partial x}$ for the Jacobian determinant and R is the potential radius (e.g. Schubert and Hack, 1983), which is related to the absolute angular momentum and defined by:

$$\frac{1}{2}fR^2 = rv + \frac{1}{2}fr^2. \tag{4}$$

Lagrangian changes in R arise solely due to drag in the azimuthal direction F_λ, namely:

$$\frac{\mathrm{D}R}{\mathrm{D}t} = \dot{R} = \frac{r}{Rf}F_\lambda\,. \tag{5}$$

Hence, R has the interesting property of Lagrangian conservation in an axisymmetric flow in the absence of mechanical forcing ($\mathbf{F} = \mathbf{0}$).

To simplify the equations further, a convenient change of coordinates consists in switching from r to R as horizontal coordinate (e.g. Shutts and Thorpe, 1978; Thorpe, 1985) and from z to θ as vertical coordinate (e.g., Schubert and Alworth, 1987). Such coordinate transformation requires that there exists a bijective mapping from (r,z) to (R,θ), which is guaranteed as long as $(f\,P) > 0$ (or simply $P > 0$ in the Northern Hemisphere), i.e. as long as the flow is stable with respect to symmetric and convective instabilities. When $P = 0$ in a region of the fluid (symmetrically

neutral flow), the area with strictly zero PV in (r, z) cross-sections collapses to a line in (R, θ) coordinates, and the coordinate transformation is no longer bijective. This special case will be further discussed in the next subsection, but let us assume $f\ P > 0$ for the remainder of this subsection.

Recalling that the Jacobian determinant represents the change in differential volume under coordinate transformation, the infinitesimal volume element is given by:

$$\mathrm{d}V = \pi \mathrm{d}r^2 \mathrm{d}z = \frac{\pi}{\frac{1}{2r}\left|\frac{\partial(R^2,\theta)}{\partial(r,z)}\right|} \mathrm{d}R^2 \mathrm{d}\theta\,. \tag{6}$$

and the corresponding mass is:

$$\mathrm{d}M = \rho \mathrm{d}V = \rho\pi\, \mathrm{d}r^2\, \mathrm{d}z = \frac{\pi}{\frac{1}{2\rho r}\left|\frac{\partial(R^2,\theta)}{\partial(r,z)}\right|}\, \mathrm{d}R^2\, \mathrm{d}\theta\,. \tag{7}$$

This relation allows us to define a potential pseudo-density (Schubert and Alworth, 1987),

$$\mu = \frac{1}{\frac{1}{2\rho r}\left|\frac{\partial(R^2,\theta)}{\partial(r,z)}\right|} \tag{8}$$

which is the density in the (R, θ) coordinate system. From the expression of P (Equation 3), we have

$$\mu = \frac{f}{P}. \tag{9}$$

Hence, using the continuity equation in (R, θ) coordinates:

$$\frac{\partial \mu}{\partial t} + \frac{1}{R}\frac{\partial(R\dot{R}\mu)}{\partial R} + \frac{\partial(Q\mu)}{\partial \theta} = 0, \tag{10}$$

we obtain the PV tendency equation in this system:

$$\frac{\mathrm{D}P}{\mathrm{D}t} = \frac{\partial P}{\partial t} + \dot{R}\frac{\partial P}{\partial R} + Q\,\frac{\partial P}{\partial \theta} = P\left(\frac{1}{R}\frac{\partial(R\dot{R})}{\partial R} + \frac{\partial Q}{\partial \theta}\right). \tag{11}$$

Another derivation of this equation, starting from Equation 2, is provided in Schubert and Alworth (1987).

It is enlightening to put the equivalence between PV and potential pseudo-density μ (Equation 9) in the perspective of the PV impermeability theorem of Haynes and McIntyre (1987). Haynes and McIntyre (1987) showed that the (Eulerian) tendency equation of the quantity $\rho P = \boldsymbol{\zeta_a} \cdot \boldsymbol{\nabla}\theta$ may be recast into a flux-form budget equation in geometric coordinates (x, y, z), here (r, z):

$$\frac{\partial \rho P}{\partial t} + \boldsymbol{\nabla} \cdot \boldsymbol{J} = 0 \tag{12}$$

with $\boldsymbol{J}$ a flux vector. On this ground, they proposed an analogy between PV and chemical substances, namely that the quantity ρP be seen as the concentration of a PV substance (PVS) of mixing ratio P. Haynes and McIntyre (1987) then proved that, contrary to fluid mass or chemical substances, there is no net flux $\boldsymbol{J}$ of PVS across isentropic surfaces even in the presence of diabatic heating and mechanical forcing. This result, named the impermeability theorem,

follows solely from the definition of PV, and does not rely on the equations of motion.

For our axisymmetric problem in $(R,\ \theta)$ coordinates, the analogous quantity to ρP is just $\mu P = f$. Hence, the impermeability theorem is expressed trivially as:

$$\frac{\partial \mu P}{\partial t} = \frac{\partial f}{\partial t} = 0. \tag{13}$$

This relation shows that $\mathbf{J}$ vanishes in $(R,\ \theta)$ space, or in other words there is no net PVS flux across either R or θ surfaces. The mass of PV substance contained within a volume delimited by iso-R and iso-θ surfaces remains constant in time.

Following Equation (13), injecting a mass of fluid within a volume delimited by iso-R and iso-θ surfaces is formally equivalent to creating anticyclonic (i.e. low) PV, whereas a removing fluid produces cyclonic PV. Such a relationship between PV and mass redistribution in rotating stratified fluids is not new. Considering the Lagrangian conservation of θ and R, Gill (1981) proposed to create anticyclones by injecting a mass of fluid at its level of neutral buoyancy in a rotating stratified flow, a method applied in tank experiments by Griffiths and Linden (1981) and a number of studies since then (e.g., Aubert et al., 2012). A similar line of reasoning was followed by Shutts et al. (1988), who used it to investigate the balanced state resulting from the inviscid and adiabatic adjustment of the atmosphere to penetrative convection. Here, we recall that this concept also applies to volcanic eruptions (as discussed by Baines and Sparks (2005), albeit from a different point of view) and to pyroconvection.

More quantitatively, if we consider an injection of fluid in a background flow of pseudo-density $\bar{\mu}$ in (R, θ) coordinates, the potential pseudo-density after the injection, μ_i, is increased due to the intrusion augmenting the mass of fluid contained within a range of R and θ. The mass fraction of injected air is simply $\chi_i = (\mu_i - \bar{\mu})/\mu_i$, i.e. the relative density anomaly with respect to the background. Then, based on the correspondence between μ and PV expressed in Equation (9), χ_i can also be written as a function of PV:

$$\chi_i(R,\theta) = \frac{\mu_i(R,\theta) - \bar{\mu}(\theta)}{\mu_i(R,\theta)} = \frac{\bar{P}(\theta) - P_i(R,\theta)}{\bar{P}(\theta)} \tag{14}$$

where $\bar{P}(\theta) = f/\bar{\mu}$ is the potential vorticity of the background state and P_{an} the relative PV anomaly with respect to $\bar{P}$. Equation (14) provides a relationship between the initial mixing ratio of a plume tracer, which is proportional to χ_i, and the relative PV anomaly:

$$P_{an} = \frac{P(R,\theta) - \bar{P}(\theta)}{\bar{P}(\theta)} \tag{15}$$

created by the injection.

3.2 | PV and tracer evolution in an inviscid flow

In the previous subsection, we proposed a possible mechanism for the initial formation of ATPs, namely the adiabatic inviscid adjustment of an injection of air from lower levels into the stratosphere. We now consider the subsequent evolution of the plume, and wish to understand the ascent of the anticyclonic vortex together with plume aerosols and trace gas anomalies. Since our work focuses on the response to the diabatic heating induced by the plume, we will neglect mechanical forcing in the remainder of this section ($\mathbf{F} = 0$).

To reformulate the problem in a simple framework, we model the plume by introducing a chemically inert La-

grangian tracer, which will be termed as A. At this point, A might represent approximately any plume tracer: black carbon aerosols, ash, water vapour, carbon monoxide, etc. The evolution of the mixing ratio χ of A is governed by an advection-diffusion equation:

$$\frac{\mathrm{D}\chi}{\mathrm{D}t} = \mathcal{D}(\chi) \tag{16}$$

where $\mathcal{D}$ is a diffusion operator (linear in χ). Ignoring tracer diffusion as a first-order approximation, the right-hand sides of Equations (2) and (16) differ in general, due to the diabatic forcing term in the PV tendency equation, which is absent from the tracer tendency equation. In fact, a joint diabatic ascent of P and χ anomalies can only take place if, everywhere where $\boldsymbol{\nabla} Q \neq \mathbf{0}$ and $\boldsymbol{\nabla}\chi \neq \mathbf{0}$, the PV cancels (in this case, this must be realized through $\boldsymbol{\zeta_a} = \mathbf{0}$). Then, the irrotational frictionless flow remains irrotational, and potential vorticity remains zero even in the presence of diabatic forcing (see Equation 2). The Lagrangian tendencies of PV and tracer mixing ratio hence coincide. While this $P = 0$ condition is consistent with the value of PV found at the core of Koobor according to ERA5 (Section 2), it is unreasonable to conceive an isolated, strictly zero-PV and tracer patch persisting over time in the presence of viscosity and tracer diffusion, which will impose continuity of the PV and A fields with the environment. Instead, in the following, we investigate the evolution of an area of non-zero (albeit small) PV (i.e., a finite injection of fluid mass) associated with a tracer plume (i.e. an injection of tracer) using the $(R-\theta)$ coordinate system.

With $\dot{R} = 0$, the general solution to Equations (11) and (16) may be obtained by solving separately for each R a couple of 1D partial differential equations (with respect to θ). We will refer to this set of 1D solutions concatenated along R as a *curtain* in the following. In each 1D domain, the Lagrangian tendencies of PV and χ are given by:

$$\frac{\mathrm{D}P}{\mathrm{D}t} = PQ_\theta \tag{17a}$$

$$\frac{\mathrm{D}\chi}{\mathrm{D}t} = \mathcal{D}(\chi) \tag{17b}$$

where $Q_\theta = \left(\frac{\partial Q}{\partial \theta}\right)_R$ and it is now understood that $\mathrm{D}/\mathrm{D}t = \partial/\partial t + Q\partial/\partial\theta$. As noted by Schubert and Alworth (1987), the solution to Equation (17b) along material (Lagrangian) air trajectories (which are known as characteristic curves in the terminology of nonlinear waves) reads:

$$P(\tau) = P_0 \exp\left(\int_0^\tau Q_\theta \mathrm{d}\tau'\right) \tag{18}$$

and highlights exponential growth/decay of the PV with time τ for constant Q_θ (with P_0 the initial PV value).

Before considering a more specific form for Q and relating it to χ, we note that, when neglecting tracer diffusion ($\mathcal{D} = 0$ in Equation 16),

$$\frac{1}{P}\frac{\mathrm{D}P}{\mathrm{D}t} = \left(\frac{\partial Q}{\partial\theta}\right)_R = -\frac{1}{\chi_\theta}\frac{\mathrm{D}\chi_\theta}{\mathrm{D}t} \tag{19}$$

where $\chi_\theta = \left(\frac{\partial\chi}{\partial\theta}\right)_R$. This relation is valid for any Q. By integrating (19) in time (τ) along characteristic curves, we obtain:

$$P\,\chi_\theta(\tau) = P(\tau=0)\,\chi_\theta(\tau=0), \tag{20}$$

i.e., that PV evolves as the inverse of the tracer gradient. Equation (20) shows that PV decreases following the flow

when the tracer gradient becomes steeper, and vice versa.

3.3 | Flow response to a heating (or cooling) tracer

We now consider the case in which the tracer A heats or cools the air. From this point on, A stands for a radiatively active specie, for instance black-carbon aerosols (which absorb sunlight) or water vapour (which increases infrared emission). Our goal is to determine how the tracer field evolves, and how this affects the PV. To the best of our knowledge, this configuration has never been considered. As a first approximation, we will assume that the anomaly in heating rate $\mathcal{H}$ induced by A is proportional to its mixing ratio χ, that is:

$$\mathcal{H} = \gamma \chi \tag{21}$$

where γ is a constant factor and the heating rate $\mathcal{H}$ corresponds to the temperature tendency $\mathcal{H} = \dot{T}$.

Equation (21) encapsulates the linear relationship between $\mathcal{H}$ and tracer mixing ratio in the case of constant and uniform radiative (and microphysical) properties of the tracer. Any substantial attenuation of the radiative fluxes, which could arise in thick plumes, is neglected. In the case of the plumes from the 2020 Australian fires, A is heating ($\gamma > 0$) and neglecting attenuation appears as a reasonable assumption, since CALIOP shows limited attenuation of the lidar beam at 532 nm (Section 2). Furthermore, regarding the radiative properties of the emitted black carbon particles, it was recently reported by Sellitto et al. (2023) that they remained stable over time scales ranging from weeks to months, which justifies using a constant γ in Equation (21). Finally, it should be mentioned that, besides simplifying the heating induced by the absorbing/emitting layer, Equation (21) also ignores the radiative damping of the temperature anomaly associated with the anticyclone (Lestrelin et al., 2021). This component is left out for now, but will be included in Section 4.

Equation (21) yields the following expression for Q:

$$Q = \dot{\theta} = \frac{\theta}{T}\mathcal{H} = \frac{\theta}{T}\gamma\chi \simeq \gamma\frac{\theta}{\bar{T}}\chi \tag{22}$$

where strictly speaking the temperature field T depends on time, R and θ, but may in practice be replaced by its background profile $\bar{T}(\theta)$. With this approximation, and after a change of the vertical coordinate to $\Theta(\theta) = \int_{\theta_{ref}}^{\theta} \bar{T}/\theta' \mathrm{d}\theta'$, Lagrangian conservation of the tracer mixing ratio in the new coordinate system (R, Θ) is expressed by a form of Burgers' equation:

$$\frac{\partial\chi}{\partial t} + \gamma\chi\left(\frac{\partial\chi}{\partial\Theta}\right)_R = K_\Theta\left(\frac{\partial^2\chi}{\partial\Theta^2}\right)_R \tag{23}$$

where on the right-hand side we have introduced a simple parameterization of $\mathcal{D}$ with $K_\Theta > 0$ a constant "diffusivity" in Θ coordinate. Burgers' equation is a canonical example of a nonlinear wave equation, and has been extensively studied (e.g., Hopf, 1950; Cole, 1951). For details, we refer the reader to standard textbooks on partial differential equations (e.g., Whitham, 1999). In Appendix A1, we present briefly the properties of the general solution to Burgers's equation initialized with a localised patch of tracer, sometimes referred to as the *single hump* solution. For small K_Θ, this solution converges towards a triangular wave, known as the asymptotic *triangular wave* solution. As explained above, this classical solution represents the evolution of the tracer profile. We also derive a solution for the associated PV profile, governed by Equation (17b). The latter aspect is specific to the present study.

We now propose to illustrate graphically the dynamics of the system. To this end, we computed the solution of the

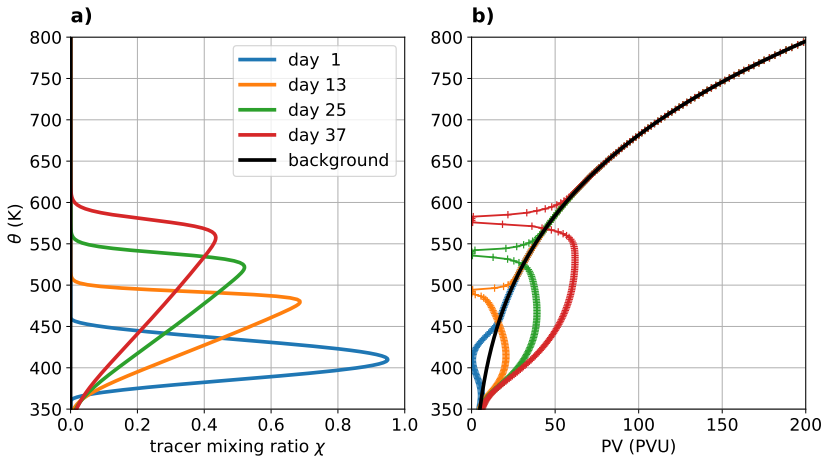

FIGURE 4 Numerical solution for the (a) tracer and (b) PV profile at the center of the structure ($R = 0$). The parameters are $\gamma = 5$ K/day/(unit tracer mixing ratio), $K_\Theta = 5$ K^2 day^{-1} , and the initial condition is given by Equation (24). The background PV profile, shown in black in panel b, is typical for mid-latitudes (constant $\bar{T} = 220$ K, $f = 10^{-4}$s^{-1}).

PV and tracer equations (Equations 16 and 17b) in (R, θ) space. The background flow is assumed at rest, so that the reference density is simply $\bar{\mu} = \bar{\rho} \Big/ \left(\frac{\partial \bar{\theta}}{\partial z}\right)_r$; we assume an isothermal profile at $\bar{T} = 220$ K (see Figure 3), representative of the extra-tropical stratosphere. The initial distribution of the tracer, χ_i, is taken equal to the fraction of the air originating from the injection (see Equation 14), and is designed to be smoothly varying in R and θ using the cosine function:

$$\chi_i(R,\theta) = 0.25(1-\epsilon)\left(1+\cos\left(\frac{\pi r}{R_{max}}\right)\right)\left(1-\cos\left(\frac{2\pi(\theta-\theta_{min})}{\theta_{max}-\theta_{min}}\right)\right) \text{ if } R < R_{max} \text{ and } \theta \in [\theta_{min}, \theta_{max}]$$
$$= 0 \text{ otherwise} \tag{24}$$

and P_i follows from Equation (14). Motivated by the main 2020 Australian vortices, we take guidance from the ERA5 reanalysis on 9 January 2020 to set the magnitude and size of the injection in (R, θ) coordinate. This suggests $R_{max} =$ 180 km and $\theta_{min} = 380$ K and $\theta_{max} = 440$ K (not shown). The amplitude, $0.25(1-\epsilon)$, with $\epsilon \ll 1$, is such that the maximum value of the tracer distribution (reached for $r = 0$ and $\theta = (\theta_{min} + \theta_{max})/2$) is $\chi_i = 1 - \epsilon$, and corresponds to a nearly vanishing PV ($P_i = \bar{P}(1-\chi_i) = \epsilon$). ϵ represents the mass fraction of environmental air mixed with the plume. It is tiny at the core of the intrusion when the pseudo-density of the background at the detrainment level is low, even for a limited amount of injected fluid. This point will be discussed further in Section 5. In practice, we use $\epsilon = 5 \cdot 10^{-2}$.

Figure 4 displays the time evolution of the tracer and PV profile at the center of the ATP ($R = 0$). Over 37 days of simulation, the symmetrical, smooth initial bulge of the tracer profile gradually transforms itself into a strongly asymmetrical triangular wave. At the top of the cloud, the tracer slope initially steepens until it stabilizes as a sharp tracer front. Note that this collapse of the tracer cloud onto a front occurs in θ coordinate, which does not mean that a similar collapse occurs in z coordinate, but rather that the lapse rate in that region is close to adiabatic. At the bottom, the tracer gradient continuously decreases, leading to the formation and deepening of a long tail (Figure 4 a). The resulting sawtooth pattern resembles the observed aerosol backscatter profiles in Figure 2. After its formation,

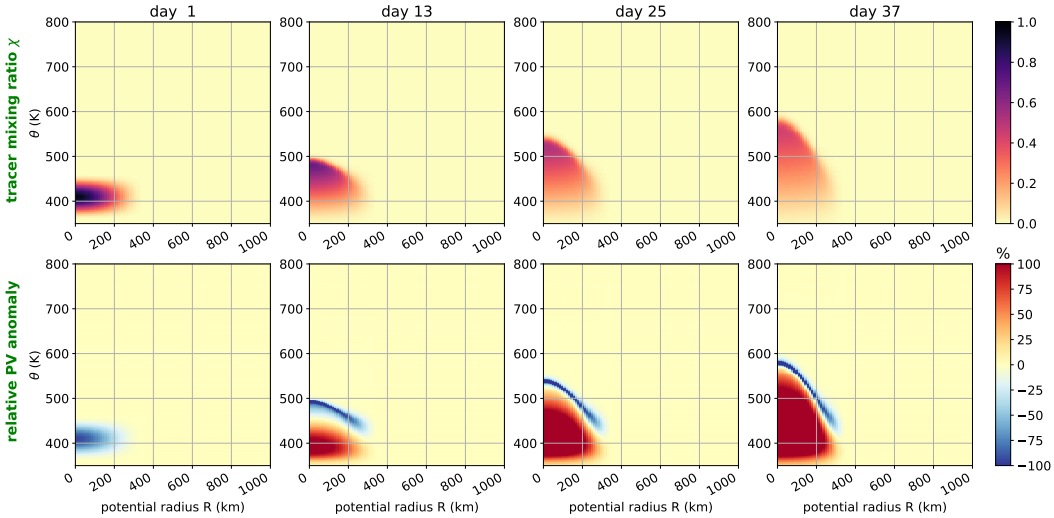

FIGURE 5 Numerical solution of a curtain of Burgers' equations along θ with $\gamma = 5$ K/day/(unit tracer mixing ratio), $K_\Theta = 5$ K^2 day^{-1}, starting from the initial condition given in Equation (24) and a background PV profile typical of the mid-latitudes. The top row shows the mixing ratio of tracer A and the bottom row shows the relative PV anomaly with respect to the background, P_{an}. Similar conditions are also used for initialisation and background in the reference WRF simulation.

the front asymptotically ascends as $\sqrt{t}$ in Θ coordinate, whereas the magnitude of the jump decays as $t^{-\frac{1}{2}}$ (Whitham, 1999). There are two processes contributing to the formation of PV anomalies. The first is the upward advection of low PV in the background profile, which always results in a negative (anticyclonic) PV anomaly, since in the stratosphere PV increases rapidly with θ. The second contribution is the Lagrangian diabatic tendency (Equation 17b). This tendency leads to a decrease of PV right at the front, bringing it to zero exponentially with time (linearly in the absence of diffusion), and to an increase elsewhere, in agreement with Equation (20). Consequently, a near-zero PV minimum ascends together with the tracer front and its magnitude increases over time both in relative terms (as $\bar{P}$ increases, $P - \bar{P}$ decreases) and absolute terms (in agreement with Equation (19), P decreases). In the tail, diabatic and advective PV tendencies are of opposite signs. A region of anticyclonic anomaly, originating in the vertical advection of both the low-PV initial condition and the background gradient, is initially maintained just below the front. It gradually shrinks, and the diabatic tendency ultimately prevails, leading to a cyclonic anomaly in the tracer tail.

Figure 5 shows a 2D representation of the tracer and PV curtains for a range of R and selected times. In each vertical column (fixed R), the tracer and PV profiles qualitatively exhibit the same evolution as the central column described above, with a tracer front ascending together with a low-PV anomaly, and a cyclonic tail behind. Quantitatively, the ascent speed of the front decreases with increasing R, due to the decreasing tracer concentration in the initial condition.

Overall, given its degree of idealisation, it is noteworthy that this analysis predicts features which are consistent with observations of ATPs, in particular

- the joint ascent of a heating tracer and anticyclonic PV anomaly,
- the formation of near-zero PV and its maintenance within the tracer cloud,

- the formation of a front at the top of the tracer cloud.

However, there is no observational evidence for the cyclonic tail, and the slowing down of the plume ascent rate over time appears faster than observed.

Besides these disagreements with the observations, the present theory is limited by strong assumptions. It relies on a preservation of the initial axisymmetry of the flow, which is not guaranteed, as we saw that the system has the intrinsic tendency to produce fronts. The $R-\theta$ approach also lacks flexibility, making it difficult, for instance, to incorporate a more realistic diabatic forcing. In particular, it is expected that radiative heating in ATPs includes significant thermal relaxation (Lestrelin et al., 2021), introducing a two-way coupling between the potential vorticity and the tracer equations. In order to determine this extra heating term within the $(R-\theta)$ framework, it would be possible to invert the temperature anomaly from PV (e.g. Thorpe, 1985), but this would not address the question of ATP stability. As an intermediate framework between analytical approaches and real-case simulations, we therefore turn to fully 3D idealised numerical simulations, in which thermal relaxation can be readily included and the validity of the underlying assumptions tested.

4 | THREE-DIMENSIONAL NUMERICAL SIMULATIONS

In this section, we study the response of the flow to an injection of the active tracer A, as in Section 3, but including more complete dynamics. Although the goal is to assess the validity of our theoretical derivation in a more realistic setting, we still use an idealised approach to bridge our theoretical results with the observations. The setup may be summarised as follows: we consider a background atmosphere initially at rest on the $f-$plane. The chosen Coriolis parameter ($f = 10^{-4}\,\mathrm{s}^{-1}$) and background stratification profile mimic the typical mid-latitude troposphere-stratosphere transition, with a tropopause located at 12 km altitude, and associated with a stratification jump in Brunt-Väisälä frequency N from $\bar{N} = 10^{-2}\,\mathrm{s}^{-1}$ to $\bar{N} = 2\times10^{-2}\,\mathrm{s}^{-1}$. At the initial time, a low-PV "intrusion" is placed in the stratosphere, collocated with a patch of the tracer A. As in the previous section, we investigate the midterm (tens of days) evolution of the flow starting from this configuration.

4.1 | Model choice and setup of the numerical experiments

The three-dimensional numerical simulations have been performed with the Advanced Research Weather Research and Forecast (WRF-ARW) model (Skamarock et al., 2008), Version 4.2.2. The model is a community model, designed for limited-area simulations of mesoscale flows. It is used operationally for weather forecasting, but also supports idealised configurations which can be flexibly used for research purposes (e.g., Bui et al., 2019; Foussard et al., 2019). Two key advantages of this model are its realism and broad range of applications and hence of validation. It is important to note, however, that there is a significant distance between the highly idealised situation considered in the previous section, and the flows that are simulated with WRF, which retains the full complexity of the compressible stratified atmosphere. Choices need to be made for the boundary conditions in the simulations. In addition, as expected with any simulations, a limited resolution will induce numerical diffusion, with possibly significant implications for derived quantities such as PV. Hence, it is not the purpose of these simulations to reproduce exactly the solutions of the very idealised model, nor the observations. Rather, they aim at identifying which features of the theoretical analysis are robust and shared with the 3D simulations, and which are not.

Our idealised set-up has open lateral boundary conditions, a free-slip lower boundary condition and a 15 km-deep sponge layer at the top of the 55-km deep domain. Since we are interested in the dry stratospheric flow, no microphysics parameterization is included. The horizontal grid is regular in Cartesian coordinates, with the consequence that axisymmetry cannot be strictly conserved. Hence, even in the absence of azimuthal perturbations at the initial stage, non-axisymmetric instabilities have the potential to develop, and the simulations may be used to assess the stability of the axisymmetric flow. The horizontal resolution is 15 km whereas the vertical levels are approximately regularly spaced in altitude, corresponding to a vertical resolution of 300 m between 10 and 38 km (the range of altitude of interest). The domain extends from the surface to about 55 km altitude and spans about 3,800 km in the zonal and meridional directions, which amounts to $256\times256\times161\simeq10^7$ grid points.

To represent radiative processes acting during the maintenance stage of the plume, we use a simple approach, and consider the heating tracer A, but also include radiative damping in the form of Newtonian relaxation. Again, the mixing ratio χ of A is conserved following the flow, except for numerical and explicit diffusion, and follows Equation (23) but with this time $\mathcal{D}(\chi)$ standing for an (anisotropic) 3D diffusion operator, which includes both parameterized and numerical contributions. In the default model configuration, a horizontal Smagorinsky first-order closure (Smagorinski, 1963) handles diffusion in the horizontal, whereas in the vertical a second-order diffusion scheme with constant diffusivity equal to 0.1 $\mathrm{m}^2\,\mathrm{s}^{-1}$ is employed. Newtonian cooling dampens deviations of the temperature from its reference

TABLE 1 List of simulations presented in this paper and values of the parameters varied across the simulations, namely the heating rate coefficient per unit tracer mixing ratio γ and the temperature relaxation timescale $\tau_r = 1/\alpha$ (Equation (25)), the altitude of the tracer injection and the presence or absence of a PV anomaly associated with the tracer anomaly. The last two columns present the fraction of total mass of the tracer A contained within regions where its mixing ratio is larger than 0.5 kg kg^{-1} ($F_{\chi>0.5}$), right after the initial adjustment and after 18 days of simulation. Thus, $F_{\chi>0.5}$ is a proxy of the dilution of the tracer plume. Simulations UP-REF and DOWN-REF are presented in Section 4. The sensitivity simulations NO-RELAX and UP-NOPV are presented in Section 5.

simulation	injection	initial	γ	$\tau_r = 1/\alpha$		$F_{\chi>0.5}$	$F_{\chi>0.5}$
name	altitude (km)	PV anomaly	(K/day)	(days)		day 1	day 19
UP-REF	15	yes	5	7	reference simulation	78%	45%
DOWN-REF	35	yes	-5	7	tracer-induced cooling	69%	32%
NO-RELAX	15	yes	5	∞	no Newtonian cooling	78%	36%
UP-NOPV	15	no	5	7	no initial PV anomaly	78%	24%

profile $\bar{T}(z)$. The full heating rate $\mathcal{H} = \dot{T} = \frac{T}{\theta}Q$ is given by:

$$\mathcal{H} = \gamma\chi - \alpha(T - \bar{T}(z)) \tag{25}$$

where γ is the heating (or cooling) rate per unit of tracer mixing ratio, and α the temperature relaxation rate. Notice that, in our simulations, α is uniform and does not depend on the tracer concentration.

Table 1 summarizes the simulations presented in this paper, all of them performed on a $f-$plane and started from an axisymmetric initial state. Different values of γ were tested. In the smoke vortex case (UP-REF simulation), it is chosen to roughly match the observed ascent rate of the Koobor plume (as seen, e.g., in Khaykin et al., 2020) at initialisation. The radiative damping rate is estimated from ERA5 to be of the order of $\alpha = 1/7\,\text{day}^{-1}$ (Lestrelin et al., 2021).

4.2 | Model initialisation

The initial state, similar to that used in Section 3, is given in $(R-\theta)$ coordinates by Equation (24). In practice, it is achieved in model coordinates by starting from an atmosphere at rest (i.e., $v = 0$). In this case $r = R$, μ is equal to the isentropic density in $r-\theta$ coordinates, and pressure, geopotential and potential temperature profiles can be derived from $\mu(\theta)$ by integrating the hydrostatic balance equation numerically in each column of the model. Instead of starting from a state of rest and letting the flow adjust to reach the cyclo-geostrophically balanced state corresponding to the initial geopotential and temperature perturbation, we could have directly initialized the simulation with a balanced vortex structure in (r,z), determined from the PV distribution in (R,θ) coordinates using an inversion approach similar to that of Thorpe (1985). However, besides its simplicity, our procedure has practical advantages; notably, it is consistent with the discretized equations of the model, and can be easily applied to more complex background flows, such as sheared flows. This flexibility comes at some additional computational cost, as a small model timestep (30 s) is required for numerical stability during the adjustment process.

In the simulations, the adjustment triggers a substantial emission of gravity waves. After a spin-up of about 2 days, the balanced state which is left consists of an upper level anticyclone, in agreement with the theoretical study of extratropical penetrative convection by Shutts et al. (1988). All times below are defined with respect to the end of

the 2-day spin-up.

Figure 6 depicts the flow on day 1, at the end of the adjustment. To a good approximation, it is in gradient wind balance and consists of an elliptical vortex with a wind anomaly of $\sim 15\ \mathrm{m\,s^{-1}}$ sandwiched within a temperature anomaly dipole of amplitude ± 5-6 K. The size of this vortex is comparable to that of Koobor (Figure 1), with a vertical depth $H \simeq 4$ km and a diameter $L \simeq 1,000$ km. The aspect ratio $H/L \simeq 4 \times 10^{-3}$ is close to the value predicted by Charney's quasi-geostrophic scaling ($f/\bar{N} = 5 \times 10^{-3}$), although the vortex, with its vanishing PV, is very far from geostrophy. Hassanzadeh et al. (2012) and Aubert et al. (2012) proposed another formula for the aspect ratio of an elliptical vortex embedded in a Boussinesq fluid at rest with background Brunt-Väisälä frequency $\bar{N}$ and in gradient wind balance with the environment, which is given by:

$$\frac{H}{L} = \frac{1}{2}\left(\frac{f^2 - \zeta_v^2}{\bar{N}^2 - N_v^2}\right)^{\frac{1}{2}} \tag{26}$$

where ζ_v and N_v are the vertical component of the absolute vorticity and the Brunt-Väisälä frequency inside the vortex, respectively. For a low absolute PV vortex ($\zeta_v \simeq 0$), Equation (26) can be rewritten:

$$\frac{H}{L} = \frac{f}{2}\left(\frac{g}{T_v}\left(\frac{\partial T'}{\partial z}\right)_v\right)^{-\frac{1}{2}} \tag{27}$$

with $T_v \simeq 220$ K the (unperturbed) temperature at the middle of the vortical structure and $\left(\frac{\partial T'}{\partial z}\right)_v \simeq \frac{12}{3.5\,10^3} \simeq 3.4 \times 10^{-3}\ \mathrm{K\,m^{-1}}$ the lapse rate anomaly within the vortex. The value estimated from Equation (27) is in good agreement with the model's result. We note that this heuristic formula yields exactly $f/\bar{N}$ if $N_v = 0$ and $\zeta_v = 0$.

The diabatic PV tendency induced by the heating at the start of the simulation is shown in Figure 6, panel (c). It features a vertical dipole, which is consistent with theoretical expectations (see Equation (11) and Hoskins et al. (2003)), and with ERA5 data assimilation tendencies around Koobor (Lestrelin et al., 2021). This pattern initially leads to an upward translation of the PV anomaly (panel b) together with the tracer. However, we cannot prefigure the later stages solely on this basis: the flow is essentially nonlinear and, since the ascent takes place *against* stratification, it involves a sort of convection. We will now investigate the actual evolution of the structure.

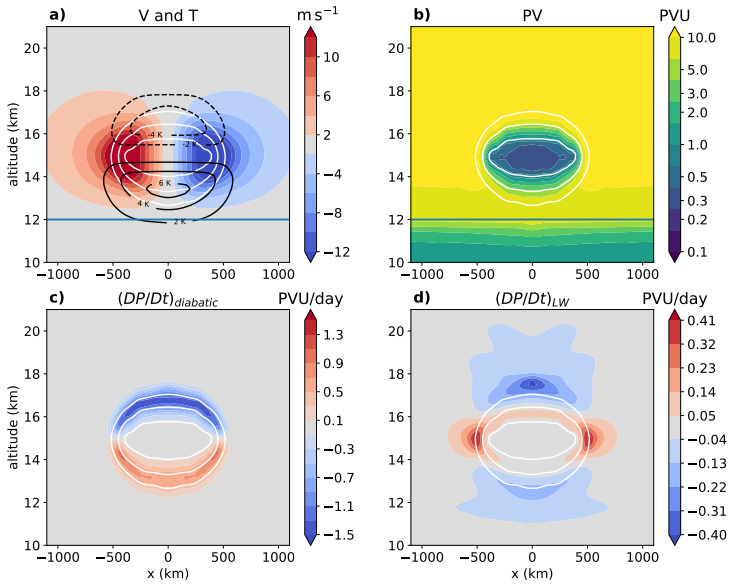

FIGURE 6 Cross-sections of (a) temperature anomaly and wind, (b) Ertel's PV through the adjusted vortex following the injection, (c) Lagrangian PV tendency due to thermal relaxation, (d) Lagrangian PV tendency due to the long wave component of heating (UP-REF simulation). White contours are isopleths of tracer *A* (0.1, 0.5 and 0.9 kg kg^{-1}).

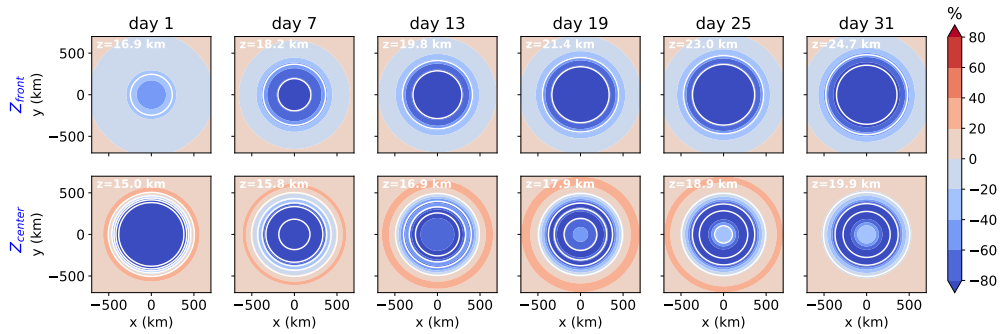

FIGURE 7 Horizontal cross-sections of PV anomaly (colours) and tracer mixing ratio (white contours: 0.1, 0.3, 0.5, 0.7, 0.9 kg kg^{-1}) at the level of (top row) the tracer front Z_{front} and (bottom row) the tracer maximum Z_{center}, as follows from the reference (UP-REF) simulation.

4.3 | Flow response to a heating tracer: ascending smoke-charged vortices

4.3.1 | Evolution in physical space

The simulations are run for 40 days following the spin-up. The first question we want to address with them is the preservation of axisymmetry. In Figure 7, we present successive horizontal charts of the tracer and relative PV anomaly P_{an}, defined by Equation (14), at the level of the plume core (centroid of the χ field) and the level of the plume front (maximum of $|\mathrm{d}\chi/\mathrm{d}z|$). The figure shows that the flow remains axisymmetric throughout the entire simulation. This property justifies the use of vertical cross-sections to provide a full account of the dynamics.

Figure 8 depicts vertical cross-sections of azimuthal wind and temperature anomaly with respect to the background (top row), and relative potential vorticity anomaly (bottom row) through the center of the domain at various times spanning the duration of the simulation. Over the first 12 days of the simulation (first 2 columns in Figure 8), the low PV and tracer anomalies rise together by $\sim$ 3 km. The tracer distribution, which is initially vertically symmetrical, quickly gains skewness with a steepening of the tracer gradients near the top of the plume and a flattening in its tail. At this stage, the pattern of the tracer cloud already resembles the backscatter ratio cross-sections through Koobor (Figure 1) and is consistent with the theory in the previous section. Similarly to the tracer, the initial negative PV anomaly ascends but also deepens over time and is enhanced near the tracer front. As a consequence, the wind and temperature dipoles are both translated upward and elongated vertically. The wind dipole initially retains a roughly constant magnitude. Regarding temperature, the cold anomaly is gradually strengthened, whereas the underlying warm anomaly becomes deeper and weaker with time. This short-term evolution of the temperature field is generally compatible with that seen in Figure 1.

As time proceeds further, while keeping an approximately constant horizontal extent, the rising tracer cloud continues to elongate along the vertical direction, with a significant ascent of the front (from $\sim$ 16 to 26 km) and a steady base. Whereas the bulk of the tracer remains located within a strong anticyclone over the entire duration of the simulation, we note that a smaller and weaker cyclonic PV anomaly develops in the lower part of the tracer cloud, and is gradually deepened and reinforced. At the same time, the pattern of the overlying anticyclonic anomaly is not simply translated, but changes from a vertically symmetric ellipsoid to a strongly asymmetric shape. On day 37 of the simulation, the low PV is located at the tracer front in the central part of the deepening cloud, but extends down on the sides (about 6 km below the central tracer front), laterally surrounding the cyclonic anomaly. At the end of the simulation, the PV field looks like a "hollow tooth", with a cyclonic PV core and an anticyclonic shell above and around

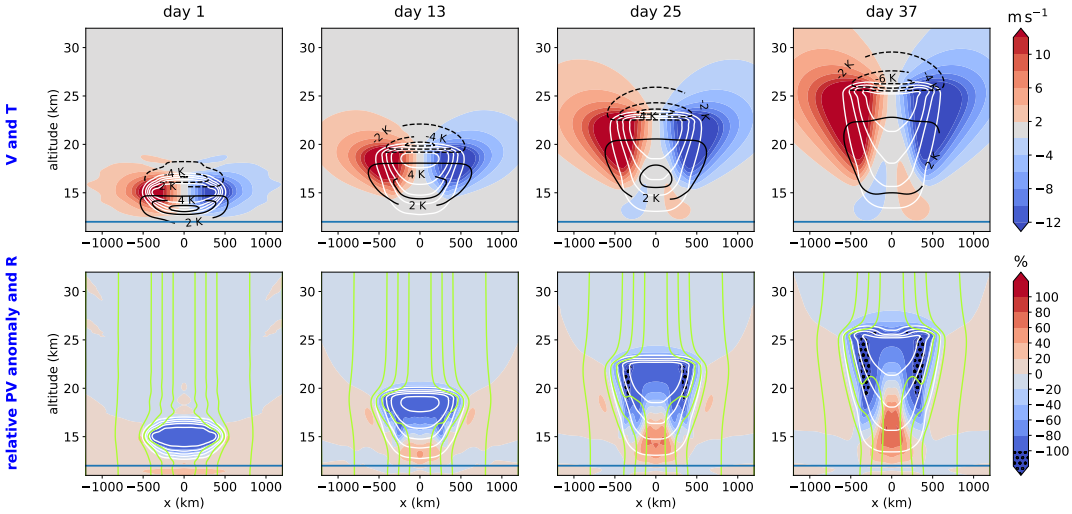

FIGURE 8 Successive cross-sections from the UP-REF WRF simulation of (top row) azimuthal wind (colours) and temperature anomaly (black contours) and (bottom row) potential vorticity anomaly from the background (colours) and potential radius R (light green contours). The area of negative absolute PV ($P_{an} < -100\%$) is hatched. White contours are isopleths of tracer A (from 0.1 to 0.9 kg kg^{-1} every 0.2 kg kg^{-1}).

it. As a result of this peculiar geometry, the cyclonic anomaly is partly shielded by the anticyclonic PV anomaly, which tends to reduce its signature on the wind and temperature fields.

Despite the formation of this cyclonic anomaly, it seems visually that most of the tracer remains confined within the anticyclone. In order to quantify the dilution of the plume and mixing with environmental air, we computed the fraction of the total mass of the tracer contained in regions with mixing ratio larger than 0.5, denoted as $F_{\chi>0.5}$. $F_{\chi>0.5}$ is a proxy for plume dilution. At the beginning of the simulation, we have $F_{\chi>0.5} = 78\%$; after 18 days, it is reduced to $F_{\chi>0.5} = 45\%$ (see Table 1). This weak dilution is related to the deflection of the flow around the anticyclone during its ascent. This is illustrated in Figure 8, where the green contours represent isolines of the potential radius R (i.e., isolines of angular momentum), which approximately coincide with actual streamlines of the flow (not shown).

Overall, despite the more complex flow shown by the WRF simulation, we note qualitative similarities with Section 3 regarding the evolution of the tracer and PV fields, with the formation of a triangular wave in the tracer profile at the vortex center and an accompanying asymmetric vertical PV dipole, with an anticyclone lying above a small cyclonic tail. The preservation of axisymmetry and the qualitative agreement with the theory motivate us to analyse the PV and A fields in $(R-\theta)$ coordinates.

4.3.2 | Evolution in (R, θ) space

Figure 9 displays the same snapshots of the simulation as Figure 8, but with the fields first averaged along the azimuthal direction and transformed to $(R-\theta)$ coordinates. If radiative relaxation and viscous drag ($\dot{R}$) were completely negligible, we would expect the evolution in $(R-\theta)$ to be strictly identical to the theory. Comparing Figure 9 and Figure 5, striking qualitative similarities are found, showing the relevance of the theory to this more realistic case. In particular, switching from r to R coordinate reveals that, following constant R surfaces (green contours in Figure 8),

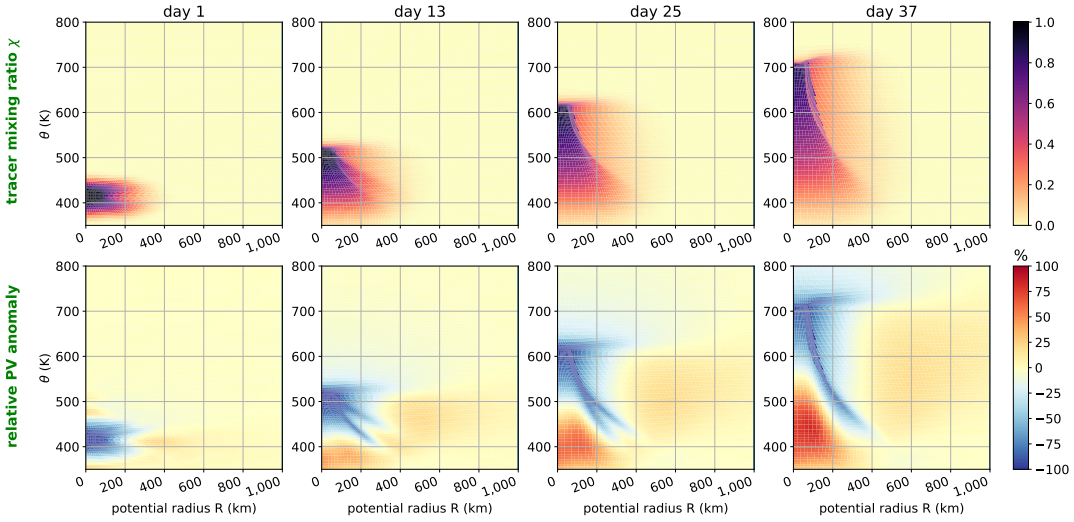

FIGURE 9 Successive cross-sections of (top row) tracer mixing ratio and (bottom row) relative potential vorticity anomaly from the background in $R - \theta$ coordinates, as follows from the UP-REF simulation.

the lateral ring of anticyclonic PV in $r - z$ (Figure 8) is actually located above the cyclone rather than around it in $R - \theta$ (Figure 9).

Consistently with Figure 5, Figure 9 shows that, in each column of the $R - \theta$ curtain, the tracer profile evolves towards a triangular wave with fronts and tails characteristic of the evolution of a localised maximum. The varying ascent speeds of the tracer fronts at different potential radii R reflect the initial value of the tracer maximum $\chi_{max}(R)$, in agreement with the theory. Some differences are already present on day 1; they are mostly related to modifications of the model fields after the initial adjustment (Figure 9) compared to the theoretical initialization (Equation 24). Those changes, which include a homogenization of $\chi_{max}(R)$ along R for $R \leq 100$ km and the generation of two fronts in θ for 100 km$\leq R \leq 250$ km, are most likely due to the unavoidable mixing and friction (i.e., diffusion of momentum) occurring during the adjustment. The evolution of these initial differences at later times can still be understood in the framework of the theory. The homogenization for $R \leq 100$ km is responsible for the straight horizontal front observed (day 25-37) in that range of R in Figure 9, whereas the double tracer front explains the transient formation of two low PV filaments (around day 13). Having a closer look at the PV field, both Figure 5 and Figure 9 show initially low PV regions of the flow remaining as wide low-PV areas in the short term (day 13), as expected from the maintenance property of an initially irrotational flow ($P \simeq 0$). Later on, the PV profiles become asymmetrical and tend to exhibit a distinct and isolated minimum at the tracer front (near -100 % relative PV anomaly) and a positive PV anomaly in the tail. In the range of R with initially multiple local maxima along θ, all fronts develop their negative PV anomaly before collapsing into a single one.

Besides these features qualitatively consistent between the idealised Burgers' solution (Figure 5) and the WRF simulation, there are also noticeable quantitative differences. The decrease in the tracer maximum is faster, and hence the ascent rate slower in the theoretical solution than in the WRF integration. Whereas both figures highlight a PV dipole, the anticyclonic PV anomaly is quickly (15 days) confined to the front in the case of the Burgers' solution but remains spread out around the front in the 3D simulation. The respective roles of radiative damping and viscous drag in those differences are discussed in the following subsection.

4.4 | Effects of radiative relaxation and friction

The comparison between the solution to Burgers' equation and the UP-REF simulation revealed an overestimation of the extent and magnitude of cyclonic PV anomalies in the theoretical model, and a more localized anticyclonic PV. We expect that this discrepancy partly results from neglecting radiative relaxation in the derivation of the equivalent Burgers' equation. The potential mechanism is illustrated in Figure 6 (panel d), which shows that, by redistributing heating over a deeper layer, the radiative relaxation tends to produce a negative PV tendency above and below the plume, far beyond the area where the tracer lies, extending the localized negative PV tendency induced by the tracer only. Qualitatively, we expect that the distribution of the heating over a deeper layer when radiative damping is included tends to slow down the sharpening of the tracer front, partly shield the tracer cloud and thus limit dilution during the ascent.

To assess the impact of radiative relaxation within the theoretical framework, we attempted to include the additional heating term in Q due to Newtonian relaxation and built a more complete numerical model solving Equations (17b) and (16). This new model requires inverting the temperature anomaly distribution from the PV field to estimate thermal relaxation; for internal consistency, this is achieved without any information from the WRF simulation but instead using a quasi-geostrophic (QG) ansatz and assuming a typical horizontal scale λ_h ($\lambda_h = 250$ km) of the structure. The model also includes explicit diffusion in the PV equation for stability. A full description of the 1D model is provided in Appendix A2. For quantitative comparison, it is initialized from the axial profile of tracer and PV of the UP-REF simulation after the 2-day spin-up.

Sensitivity calculations with this 1D model confirm that increasing the temperature relaxation rate α slows down the decay of the maximum tracer mixing ratio and therefore increases the vertical ascent rate of the front, although without preventing its formation. Decreasing the horizontal scale λ_h reduces the amplitude of the temperature anomaly and shallows its vertical scale. While we restricted ourselves to a range of tracer diffusivities K_θ low enough such that diffusion only marginally affects the results (in particular the decay of the tracer maximum or its propagation speed remain insensitive to this parameter), this term still controls the width of the tracer front. Figure 10 compares the evolution of the tracer, PV and temperature profiles in the WRF UP-REF simulation with integrations of the 1D model for an adjusted set of parameters ($\gamma = 5$ K/day/(kg kg^{-1}), $1/\alpha = 5$ days, $K_\theta = 17$ K^2/day, $\lambda_h = 250$ km, see Appendix A2). In both cases, the shape of the tracer resembles a triangular wave, with similar peak values. The distribution of PV also depicts a relatively good agreement between the two approaches, from shorter times, when the low PV cloud is preserved, to longer times, in particular regarding the sharpness of the PV minimum located at the front. The PV jump behind the front is larger in the 1D model.

Another difference with the WRF simulation lies in the evolution of the amplitude of the negative temperature anomaly. It is decaying over time in the 1D model (by a factor of 2 over the course of the integration), but tends to grow in the WRF simulation. This may be related to the assumption of a constant horizontal scale λ_h in the QG inversion. The 3D simulation (Figure 8) actually shows a lateral expansion of the anticyclone with time, and increasing λ_h would indeed increase the amplitude of temperature anomaly. This decrease of the temperature anomaly ahead of the front likely explains the need for an increased value of α in the 1D model.

In order to assess the effect of radiative relaxation in the complete 3D simulations as well, we performed another numerical experiment with Newtonian relaxation switched off (NO-RELAX). Its early evolution is qualitatively similar to UP-REF, but the area of anticyclonic PV becomes significantly shallower and the positive PV is significantly larger. Due to the lack of shielding of the plume by the relaxation-induced part of the Q field, the dilution of the tracer in NO-RELAX is also increased compared to UP-REF, in agreement with the 1D model results. After 18 days, $F_{\chi>0.5}$ reduces to 36% (vs 45% in the presence of relaxation, Table 1). At later stages, this smaller tracer mixing ratio leads

to a slower ascent, which is again consistent with the effect of the α parameter in the 1D model. Overall, this points to an important role of the longwave radiative transfer in the dynamical evolution of the anticyclone. Here, we only included a simplistic parameterization of radiative relaxation with uniform damping parameter, which only accounts for the temperature anomaly. The impact of the complex mixture of compounds radiatively active in the infrared contained in wildfire plumes, including both black carbon aerosols and greenhouse gases (water vapour, etc.), or of a depletion in other species (ozone), remains to be assessed.

Besides radiative relaxation, some differences between the theory and the WRF simulation must be a consequence of the diffusion of momentum generating a cross-R flow. In particular, in the 3D simulation, the top of the tracer front exhibits a protrusion towards large R (Figure 9). This protusion corresponds to the tracer ring above the main plume in Figure 8. Such a feature cannot occur from an inviscid evolution of the initial condition. We interpret this protrusion as resulting from a drag occurring at the top of the vortical flow where the vertical derivative of the balanced azimuthal wind is the largest, leading to positive $\dot{R} = (r/R)F_\lambda$. As a proxy for drag, we examined the distribution of regions of low Richardson number (not shown), which indeed emphasise both the shallow front and the lateral tail of the tracer cloud as regions with likely significant turbulence/mixing. The global impact of friction may also be grasped by considering the integral of Equation (10) along θ: only mechanical forcing can result in mass fluxes across iso-R surfaces ($\dot{R} \neq 0$). Over the course of the simulation, the mass of air enclosed within $R < 100$ km and 360 K$< \theta <$ 800 K is reduced by 30%, demonstrating significant viscous drag effects which are not captured in the 1D- framework. This effect is even larger for the flux of A, emphasising either an enhanced exchange of mass through in regions of high tracer content, or the existence of cross-R diffusion of A. Overall, this suggests a significant role of parameterized and numerical (e.g., associated with the Cartesian geometry of the grid) drag in the evolution of anticyclonic plumes, an effect which cannot be accounted for in a purely 1D framework. This process may be associated with dynamic instabilities, but they do not generate a breaking of the axial symmetry at the resolution of the simulations.

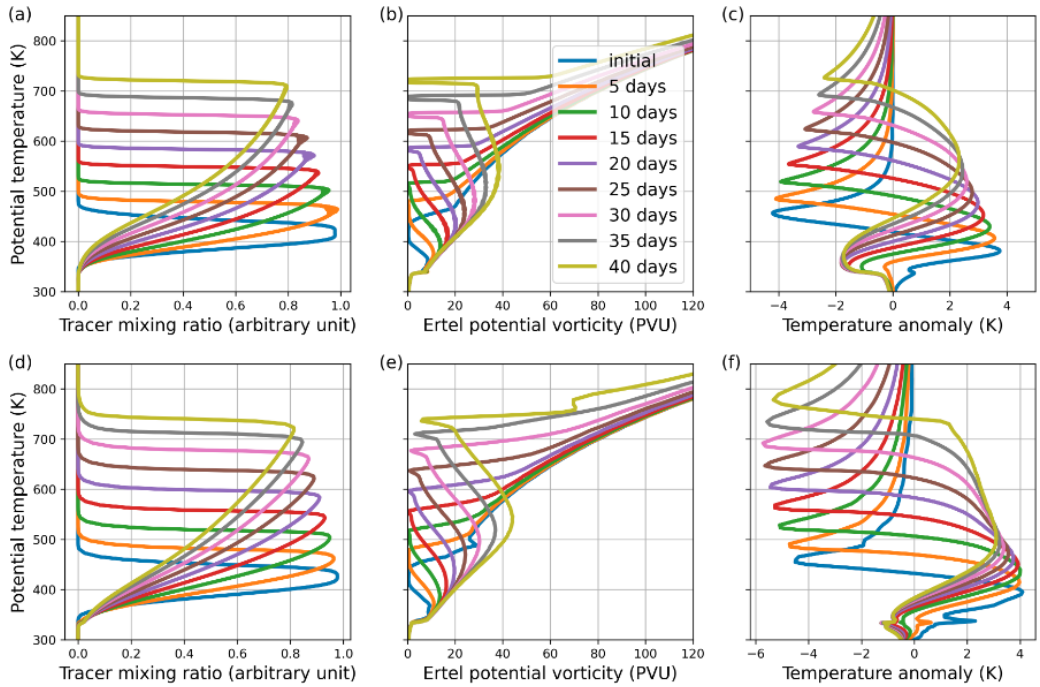

FIGURE 10 Profiles of (a, d) tracer mixing ratio, (b, e) potential vorticity and (c, f) temperature anomaly. Panels (a), (b), (c) correspond to numerical integration of Equations (17b) and (16) with the diabatic heating defined by Equation (25) and the temperature inverted using the formula provided in Appendix A2 with $\lambda_h = 250$ km. Panels (d), (e) and (f) are average profiles for $0 \leq R \leq 60$ km in the UP-REF simulation.

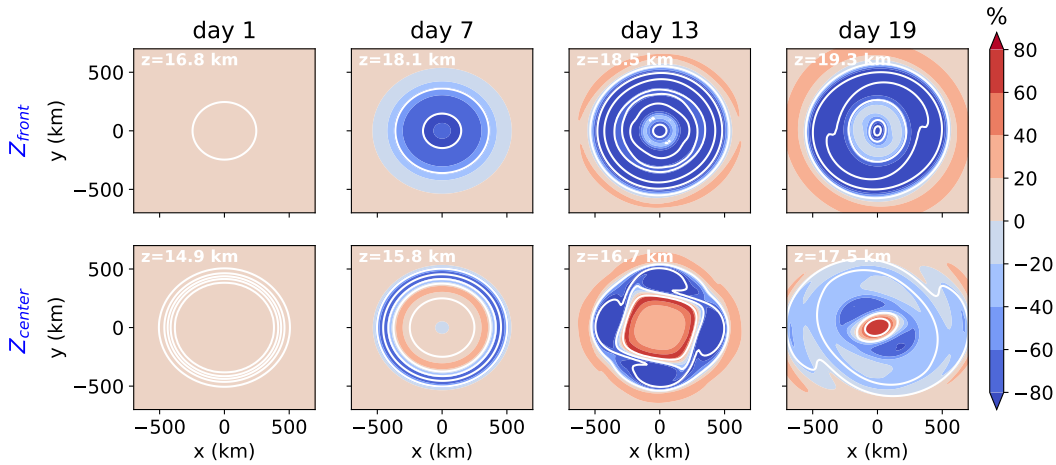

FIGURE 11 Horizontal cross-sections from the UP-NOPV simulation of PV anomaly P_{an} (colours) and tracer (white contours: 0.1, 0.3, 0.5, 0.7, 0.9 kg kg^{-1}), at the level of (top row) the tracer front and (bottom row) the tracer maximum.

5 | DISCUSSION

5.1 | Isolation of the plume from environmental air: impact of low PV initialisation

A special property of the ascending plumes is their sustained isolation from the environment. It might have been expected that radiative instabilities driven by the heating result in significant mixing between the plume and the environment. We have seen that this is not the case, for two reasons. First, the presence of a low PV anomaly is associated with streamlines avoiding the tracer cloud, thus preventing its dilution within background stratospheric air (Section 4.3). Second, the additional heat transfer provided by the longwave relaxation of the temperature perturbation associated with the PV anomaly shields the tracer cloud and reduces mixing with outside air. In the absence of an initial PV anomaly, there is no temperature anomaly and this shielding is absent at the beginning of the simulations.

Thus, it is expected that the co-injection of a heating tracer and of 'air', resulting in a plume initially trapped within a low absolute PV anticyclone, plays a key role in preventing dilution of the tracer along the ascent through the effects of both dynamical isolation in a low PV vortex and thermal relaxation. However, a few previous studies (e.g., Doglioni et al., 2022) have reported on simulations of ATPs without including an initial PV anomaly. In order to test the impact of this parameter on the evolution of the plume, we performed a simulation including the same initial tracer field as UP-REF but not the initial PV anomaly (simulation UP-NOPV). As shown in Figure 11, an anticyclone still does form at the level of the tracer front in this simulation. However, it only encompasses a small fraction of the tracer plume after 2 weeks. As a result, the dilution of the tracer is larger in this simulation: after 18 days, $F_{\chi>0.5} = 24\%$ (compared to 45% in the UP-REF simulation, 36% in the NO-RELAX simulation). Contrary to the case with a co-injection of mass, the initial axisymmetry of the plume is not maintained. On the contrary, we observe a destabilization of the initially axisymmetric flow. Whereas there seems to be a relaxation towards axisymmetry at later times, the anticyclonic plume trapping is still weak on day 19 of the simulation.

The difference between cases with and without initial mass injection is reduced when we consider an absorbing tracer injection below the tropopause, between 10 and 12 km, as used by Doglioni et al. (2022) (not shown). Although

a breaking of the axisymmetry of the flow still occurs, large anticyclonic PV anomalies are created by the diabatic tropopause crossing, and they tend to more rapidly merge (within less than two weeks) than when the tracer is directly introduced in the stratosphere.

In realistic dynamical settings, including vertical shear and large-scale deformation, we expect that the initial presence of collocated low PV anomalies will prevent the rapid dilution of the tracer both below and above the tropopause and enable the rapid formation of a compact plume. Even if distributed among a few patches, we speculate that the initial low PV anomaly favours the emergence of a single coherent plume through vortex merger (e.g., Dritschel, 2002; Reinaud and Dritschel, 2002). In the case of the Australian fires, several (about ten) large pyrocumulonimbii reached the stratosphere (Peterson et al., 2021) and probably later self-organised into a small number of ATPs, including Koobor.

5.2 | Environmental conditions for anticyclonic plume formation: altitude and latitude of the injection

In Section 3, we argued that the (cross-isentropic) injection of air near the level of neutral buoyancy is responsible alone for the initial formation of an ATP. From a dynamical point of view, neither the vertical gradient of potential vorticity nor the difference between tropospheric and stratospheric PV play a direct role, since Lagrangian conservation of PV does not apply. However, for a similar amount of fluid being injected, the smaller the background isentropic density σ, the larger the background PV and the relative PV anomaly. Given the background profile of PV (see Figure 4), it comes with no surprise that anticyclonic plumes are more likely to occur higher up in the atmosphere, where the fluid is lighter and more stratified. This likely explains why ATPs have not been reported after tropospheric injections.

A second factor regarding the initial formation is the latitude of the injection. This important parameter has been ignored so far in our investigations adopting the f-plane approximation. We expect that the efficiency of the anticyclonic confinement depends on the ratio of the relative vorticity (equal to $-f$ if $P \simeq 0$) to the change in planetary vorticity between the center and the edge of the structure. In polar and mid-latitude regions, encountering quasi-zero PV is extremely rare, and the $P \simeq 0$ vortex provides strong isolation. In contrast, in tropical regions, ambient PV is closer to 0 and the isolation provided by low PV is limited.

The non-dimensional number comparing the magnitude of latitudinal vorticity variations to the local vorticity anomaly ($\simeq -f$ in a zero-PV vortex) is $(\beta L)/|f|$ where $\beta = (2\Omega/a)\cos(\phi)$ ($a = 6,400$ km is the planetary radius, ϕ the latitude and $\Omega \simeq 7.27 \times 10^{-5}$ s^{-1} the Earth rotation rate) and L is the horizontal scale of the vortex. Assuming that the typical horizontal size of the structure L is of the order of the Rossby radius of deformation radius R_d, as suggested by its aspect ratio, we have:

$$\frac{\beta L}{|f|} = \frac{\beta R_d}{|f|} = \frac{\beta N H}{f^2} = \frac{N H}{2\,\Omega a \sin\phi \tan\phi} \tag{28}$$

For an injection of depth $H \simeq 1$ km in the stratosphere ($N \simeq 2 \times 10^{-2}$ s^{-1}), the condition $(\beta L)/f < 0.2 \ll 1$ is satisfied poleward of about 20°. Closer to the equator ($\beta L/f > 1$), the efficiency of the trapping is reduced as the latitude shift which is necessary to reach $P \simeq 0$ on an isentropic surface diminishes. Hence, confinement within an anticyclone is weaker in tropical regions- provided it occurs. The dynamical response to heating is affected by the equatorial beta effect, as suggested for the evolution of the HTHH plume by Schoeberl et al. (2023). We leave investigations of this interesting aspect for future dedicated studies.

5.3 | The case of a cooling tracer (descending water-rich/ozone-poor plumes)

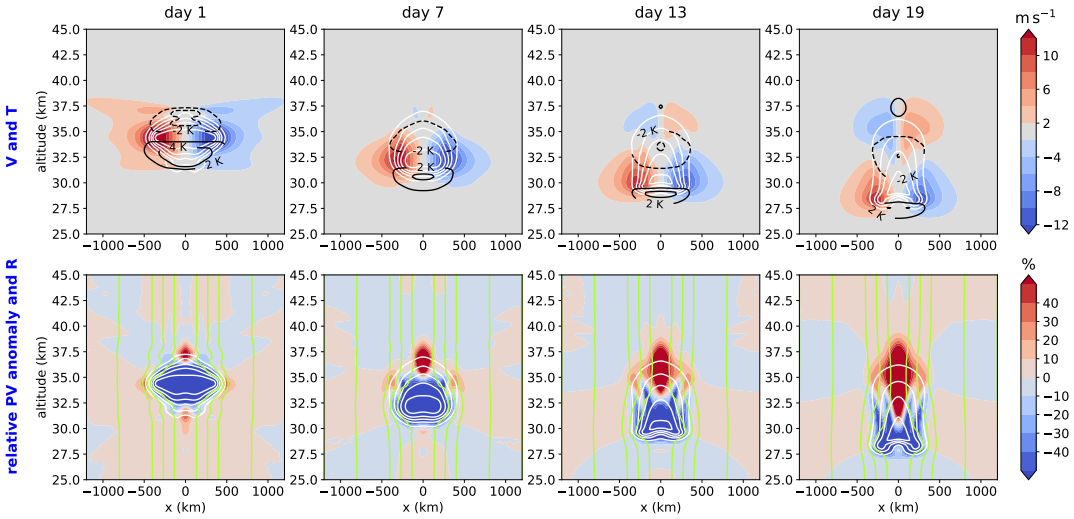

FIGURE 12 Successive cross-sections from the DOWN-REF simulation of (top row) wind (colours) and temperature anomaly (black contours) and (bottom row) potential vorticity anomaly from the background (colours) and momentum radius R (light green contours). The area of negative absolute PV ($P_{an} < -100\%$) is hatched. White contours are isopleths of A (from 0.1 to 1 every 0.1 kg kg^{-1}).

Up to now, we have been focusing on the case of a heating tracer, which was motivated by observations of stratospheric wildfire plumes. A volcanic plume reaching deep in the stratosphere can detrain large amounts of water vapour, as anticipated by, e.g., Glaze et al. (1997), and recently observed in the aftermath of the January 2022 Hunga Tonga-Hunga Ha'apai (HTHH) eruption (Millán et al., 2022; Khaykin et al., 2022a). Following the latter event, Sellitto et al. (2022) suggested that radiative cooling from the injected water vapour is likely to strongly dominate the diabatic forcing. Indeed, evidence of compact descending patches of HTHH volcanic compounds was presented in Legras et al. (2022). Motivated by this natural example, we explore the response of the stratospheric flow to a plume of tracer cooling the fluid. Contrary to the heating tracer case, however, we do not intend here to simulate a specific event. Instead, we consider the hypothetical case of a cooling tracer injected in the mid-latitude stratosphere at 35 km altitude. The cooling rate per unit tracer is now $\gamma = -5$ K/day/(kg kg^{-1}), i.e. opposite to the heated case. This magnitude of the cooling remains within the range of plausible values; for instance, Sellitto et al. (2022) estimated the cooling rate in the HTHH plume to be of the order of $\dot{T} = -10$ K/day at the day +3 stage.

Figure 12 shows the time evolution of the flow in (r, z) coordinates. Similarly to the ascending case, the tracer profile develops a front and a tail, although their vertical orientation is reversed. A fundamental difference with the ascending case is the orientation of the motion with respect to the background PV (and density) gradient. This results in the faster dilution of the tracer in denser air in (R, θ) space (Equation (16)) and its contraction in physical space. Quantitatively, $F_{\chi<0.5}$ decreases from 70% after the adjustment to 32% after 18 days of simulation, slightly faster than in the ascending case (Table 1). Due to its downward advection into a lower PV environment, the magnitude of the anticyclonic PV anomaly reduces over time, whereas that of the positive PV anomaly grows. The effect of advection is here opposite to the ascending case and limits the development of the anticyclonic anomaly. Nevertheless, this

experiment shows that a cooled vortex may also persist during its descent and form a long-lived ATP.

6 | SUMMARY AND CONCLUSIONS

Diabatically forced anticyclonically trapped plumes (ATPs) were discovered in the extra-tropical stratosphere following the extreme 2019-2020 Australian wildfires. The largest of these Australian ATPs, a 1,000 km-diameter, radiatively heated vortex nicknamed Koobor, was observed to ascend from 18 to 35 km. More recently, the plume of the 2022 Hunga Tonga-Hunga Ha'apai eruption underwent a spectacular diabatic descent due to the cooling induced by an extreme water vapour anomaly. In that case, satellite observations suggested the presence of a vorticity anomaly colocated with the tracer plume. By hindering the dilution of the plumes, vortical structures increase their longevity and modify their impact on radiation, chemistry, and dynamics. From the point of view of geophysical fluid dynamics, these ATPs exhibit several peculiarities, such as a virtually-zero potential vorticity maintained at the center of the 2020 Koobor vortex according to the ERA5 reanalysis.

In this study, we adapted a theoretical framework developed for tropical cyclones (Schubert and Alworth, 1987) to investigate the dynamics of potential vorticity in diabatically forced axisymmetric anticyclones on the f-plane. Based on an extension of the impermeability theorem of Haynes and McIntyre (1987), we argued that the creation of anticyclonic PV in ATPs occurs concomitantly with the injection of a mass of air directly into the stratosphere by pyroconvection or volcanic eruptions. The formation of large ATPs may additionally involve the merging of a number of distinct initial anticyclones, through vortex merger.

The subsequent evolution of an ATP over timescales ranging from weeks to months is controlled by radiative heating or cooling within the plume. At first order, radiatively active species, such as sunlight-absorbing aerosols or infrared-emitting water vapour, can be represented by a chemically inert tracer heating or cooling the air at a rate proportional to its mixing ratio. If the active tracer is initially located within a patch of exactly zero absolute PV, the Lagrangian tendencies of PV and tracer become the same, and we expect their coincidence to be maintained over time. Considering the more realistic case of a low, but non-zero initial PV colocated with the tracer, the problem is greatly simplified by switching from cylindrical coordinates to angular momentum-potential temperature coordinates. Then, neglecting radiative relaxation, the diabatic motion of the tracer reduces to a variant of Burgers' equation, whereas PV passively follows the tracer evolution. The dynamics of Burgers' equation leads to the formation of a vertically asymmetrical tracer cloud, with a sharp front ahead of the plume (i.e., at its top for heated vortices) and a smoothly sloping tail at its rear. In the case of a heating tracer, this pattern is reminiscent of CALIOP backscatter ratio cross-sections through Koobor. Near the tracer front, anticyclonic PV is sustained, whereas the tail is associated with cyclonic PV. While the joint ascent of the anticyclonic PV and tracer plume is consistent with the observations, the cyclonic tail predicted by this theory is not present in the case of Koobor according to the ERA5 reanalysis.

To assess the validity of the theory, we performed more complete numerical simulations with the Weather Research and Forecast (WRF) model, including Newtonian relaxation of the temperature anomalies in the heating rates. The simulated flow remained axisymmetric, and showed qualitative agreement with the theoretical picture regarding the evolution of both tracer and PV. In particular, despite the larger extent of the anticyclonic PV, which encompasses most of the tracer plume, a cyclonic PV anomaly still develops in the tail of the plume. This cyclone is smaller and weaker than the overlying anticyclone, and appears partly shielded by the anticyclonic PV anomaly. Furthermore, a sensitivity simulation demonstrated that the inclusion of Newtonian cooling tends to weaken this cyclonic anomaly. Radiative relaxation of temperature perturbations also stabilizes the anticyclonic structure and reduces the mixing of the plume with environmental air. Consistently, introducing a low PV anomaly together with the tracer at the begin-

ning of the simulations was found to favour the persistence of a compact plume and to preserve it from dilution as it ascends through the stratosphere. Compared to the inviscid theory, the WRF simulations also emphasise the role of diffusion of momentum, secondary in the beginning but significant for the long-term evolution of ATPs. The effect of mechanical forcing can be directly quantified in (R, θ) and this aspect deserves further dedicated investigations.

Several processes were ignored in our set-up. Notably, vertical shear of the horizontal wind may play a key role in the evacuation of the cyclonic tail and the maintenance of the ellipsoidal shape of the anticyclone. Variations of the Coriolis parameter influences the latitudinal drift of the anticyclone and the evolution of tropical plumes. Other crude simplifications concern the radiation and, for absorbing particles, aerosol microphysics. The parameterised radiative heating/cooling rate did not vary in time, and more importantly, depends linearly on the tracer mixing ratio. While we do not expect diurnal variations of the heating to have a strong impact on the overall-balanced plume, nonlinearities in the heating function (e.g. saturation above a given tracer concentration) could strongly affect the dynamics. Regarding microphysics, the vertical motion of the tracer was assumed purely Lagrangian, which is well-adapted to gases but fails to describe the sedimentation of aerosol particles over the course of a few months, even if slow. The respective roles of these different processes should be assessed in future work. Extreme wildfires are expected to become more frequent in the coming decades due to climate change. Meanwhile, there are important stakes around understanding volcanic perturbations of the stratospheric aerosol layer due to the need to assess the potential effects and likely risks of stratospheric geoengineering. In this context, it is crucial to better constrain the dynamical behaviour of stratospheric volcanic and wildfire plumes as a prerequisite to reliably quantifying their long-term impact on ozone chemistry, stratospheric circulation and global climate.

A1 | APPENDIX: PROPERTIES OF THE COUPLED PV-TRACER SYSTEM

A1.1 | Solution of the coupled PV-tracer system without diffusion

In the limit of vanishing diffusion ($K \to 0$), Burgers' equation can be solved along characteristic curves and the solution to Equation (17b) can be obtained using the identity in Equation (20). Starting from an initial value $(\chi_\theta)_0$ of the tracer slope along a characteristic curve and an initial background temperature $\bar{T}_0$, χ_θ evolves over time (τ) as:

$$\chi_\theta(\tau) = (\chi_\theta)_0 \, \frac{\bar{T}_0/\bar{T}}{1 - (\tau/\tau_s)} \tag{A1}$$

whereas potential vorticity P follows:

$$P = \left(1 - \frac{\tau}{\tau_s}\right) \frac{\bar{T}}{\bar{T}_0} P_0 \tag{A2}$$

with $\tau_s = -(\gamma\,(\chi_\theta)_0\,\theta_0/\bar{T}_0)^{-1}$ and $\bar{T}_0$. On the upper side of the tracer cloud ($\gamma\,(\chi_\theta)_0 < 0$), the nonlinear advection term causes a singularity (multivalued tracer profile) to occur at τ_s. At this point, characteristic curves intersect and the PV reaches zero, which corresponds to shocks and overturnings in the physical system. Formally, it is still possible to construct physically acceptable ("vanishing viscosity") discontinuous solutions to the tracer equation (Whitham, 1999). They asymptotically converge towards the triangular wave solution, which exhibits a tail and an abrupt jump. The magnitude of the discontinuity decreases as $1/\sqrt{t}$, and the singularity ascends as $\sqrt{t}$. Note that the relations A3 and A2 remain valid everywhere outside the singularity, and in particular on the lower side of the tracer cloud (the fraction of the cloud upstream of the jump and where $\gamma\,(\chi_\theta)_0 > 0$).

A1.2 | Frontal PV dynamics in the presence of tracer diffusion

For finite but small enough K (compared to $\int \gamma\chi \mathrm{d}\Theta$), the formation of the singularity is prevented, and the shock is replaced by a tracer front of finite width $\Delta\Theta \simeq K/(\gamma\chi_{max})$. The front location and magnitude correspond to that of the jump expected in the $K \to 0$ limit, i.e. the triangular wave solution (Whitham, 1999). In particular, they do not depend on the exact value of K. Furthermore, as a result of Equation (18), the PV decreases exponentially in the area of the front ($Q_\theta < 0$). This behaviour is illustrated in this section for the case of a steadily propagating tracer front.

With a constant diffusivity $K > 0$, Equation (23) is the viscous Burgers' equation. It admits as an analytical solution the function:

$$\chi(\theta, t) = \frac{\chi_{max}}{2}\,(1 - \tanh(\xi)) \tag{A3}$$

which represents a steadily propagating front. In Equation A3,

$$\xi = \frac{\gamma\chi_{max}}{4K}\left(\theta - \frac{\chi_{max}}{2}\gamma t\right) + a$$

where χ_{max} is the tracer maximum (height of the front) and a an arbitrary integration constant. Here, the front has width $K(\gamma\chi_{max})$ and it is travelling at speed $\gamma\,\chi_{max}/2$. Assuming the tracer profile given by Equation (A3), the hyperbolic PV equation (17b) may be solved along its characteristic curves (here, material trajectories) for each value ξ_0.

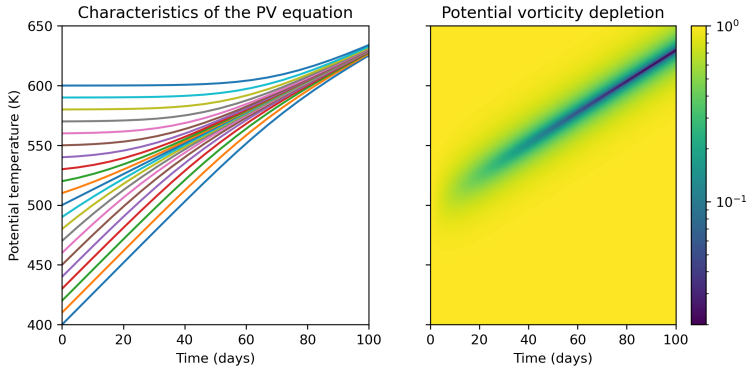

FIGURE A1 (a) Characteristic curves of the potential vorticity equation for $\gamma = 5$ K/day/(kg kg^{-1}), $K = 17$ K^{2}day^{-1}, $\chi_{max} = 1$ and a front initially at $\theta_0 = 500$ K. (b) Evolution of the potential vorticity ratio P/P_0 for these conditions.

Lagrangian variations of ξ are governed by the ordinary differential equation:

$$\frac{\mathrm{D}\xi}{\mathrm{D}t} = -\frac{(\gamma\chi_{max})^2}{(8\,K)}\tanh(\xi) \tag{A4}$$

with solution $\sinh\xi = \sinh\xi_0 \exp\left((\gamma\chi_{max})^2\,\tau/(8\,K)\right)$, yielding the characteristic curves. Injecting into the expression of $Q_\theta = \gamma\chi_\theta$ and using the solution to Equation (17b) along its characteristic curves, we obtain the parametric solution:

$$\theta(\xi_0, t)) = \frac{4K}{\gamma\chi_{max}}\left(\frac{\chi_{max}^2\gamma^2 t}{8K} + \operatorname{arcsinh}\left[e^{-\frac{\chi_{max}^2\gamma^2 t}{8K}}\,\sinh\xi_0\right] - a\right), \tag{A5}$$

$$P(\theta(\xi_0, t), t) = P_0(\theta(\xi_0, 0))\sqrt{\frac{1+\sinh^2(\xi_0)}{e^{\frac{\chi_{max}^2\gamma^2 t}{4K}} + \sinh^2(\xi_0)}}. \tag{A6}$$

As shown in Figure A1, the characteristic curves gather in the frontal region of the tracer distribution due to the advective effect of the heating and (A6) demonstrates that PV decays exponentially to zero.

A2 | APPENDIX: COUPLED TRACER-PV 1D MODEL INCLUDING THERMAL RELAXATION

In order to assess the role of radiative relaxation, we built a 1D model solving the coupled Equation (17b) for the PV and Equation (16) for the tracer, with a diffusion accounting for the background density gradient:

$$\frac{\partial \chi}{\partial t} + Q\frac{\partial \chi}{\partial \theta} = \frac{1}{\bar{\mu}}\frac{\partial}{\partial \theta}\left(K\bar{\mu}\frac{\partial \chi}{\partial \theta}\right) \tag{A7}$$

In practice, the diffusivity for the tracer is $K = 17\,\mathrm{K}^2\,\mathrm{day}^{-1}$ and a diffusivity $K_P = 1.7\,\mathrm{K}^2\,\mathrm{s}^{-1}$ is also introduced in the PV equation to insure numerical stability. As expected, the sensitivity to diffusivity is limited over the range of values tested; in particular, it does not affect the decay of the tracer maximum at first order. The value of K for the tracer was adjusted to reproduce the width of the front observed in the WRF simulation.

The heating rate $Q = \gamma\chi - \alpha(T - \bar{T})$ used in Equation (A7) and Equation (17b) is the one introduced in WRF (defined in Equation 25) with $\gamma = 5\,\mathrm{K\,day}^{-1}/(\mathrm{kg\,kg}^{-1})$ and $\alpha = 2.2\,\mathrm{day}^{-1}$. Contrary to the case examined in Section 3, the columns are no longer independent and knowledge of the radial PV distribution is required in order to invert the local temperature profile. Here, for simplicity, we assume a constant horizontal scale λ_h for the structure, and use a quasi-geostrophic ansatz to derive a direct formula relating the temperature anomaly to the perturbation of PV in the column. Under the quasi-geostrophic approximation (Berrisford et al., 1990), the full PV is approximated as

$$P = \frac{(f+q)}{\bar{\sigma}}$$

where $\bar{\sigma} = -1/g(\partial\bar{p}/\partial\theta)_{x,y}$ is a mean vertical profile which depends only on θ and q is the quasi-geostrophic potential vorticity which is defined as

$$f\,q = \nabla_\theta^2 M + \frac{f^2}{g\bar{\sigma}}\frac{\partial}{\partial\theta}\left(\bar{\rho}\theta\frac{\partial M}{\partial\theta}\right) \tag{A8}$$

where $M = C_p T' + \phi'$ is the anomaly in the Montgomery potential with respect to the basic stratification and $\bar{\rho}$ the background density profile. q satisfies

$$\left(\frac{\partial}{\partial t} + \mathbf{v}_g\cdot\nabla_\theta\right)q = \frac{f}{\bar{\sigma}}\frac{\partial(\bar{\sigma}\dot{\theta})}{\partial\theta} \tag{A9}$$

with $\mathbf{v}_g = (-\frac{1}{f}\frac{\partial M}{\partial y}, \frac{1}{f}\frac{\partial M}{\partial x})$ the geostrophic velocity.

Based on this, we derive the temperature from the anomaly P' of the PV along the axis for which $q = -\bar{\sigma}P'$. The assumed horizontal scale λ_h is used to replace the horizontal Laplacian in (A8), i.e. $\nabla_\theta^2 M = -(1/\lambda_h^2)M$. For the sake of simplicity, we also assume a uniform background temperature $\bar{T}(\theta) = T_1$ in the vertical domain of the vortex. The explicit formula for the perturbation temperature on the axis is then:

$$T'(\theta) = \frac{T_1}{2f}\left(-\left(1+\frac{\kappa}{2\eta}\right)\int_\theta^\infty\left(\frac{\theta}{x}\right)^{\eta+\frac{1}{2\kappa}}q(x)\frac{dx}{x} + \left(1-\frac{\kappa}{2\eta}\right)\int_{\theta_T}^\theta\left(\frac{x}{\theta}\right)^{\eta-\frac{1}{2\kappa}}q(x)\frac{dx}{x}\right) \tag{A10}$$

where $\eta^2 = \frac{g^2}{\lambda_h^2 f^2 N^2} + \frac{1}{4\kappa^2}$, $\kappa = 2/7$. Note again that the temperature anomaly obtained from this QG inversion only takes the central PV profile into account and is not expected to reproduce exactly the actual evolution of the temperature

field in the WRF simulation. The value of λ_h (250 km) was chosen in order to reproduce the depth of the temperature anomaly at the initial time of the simulation. Nevertheless, the slight horizontal expansion of the vortex as it ascends is not represented in this constant-λ_h framework, and the agreement between WRF and 1D-model temperature anomaly deteriorates over time. To circumvent this issue and better reproduce the evolution of the tracer field seen in the WRF simulation with the 1D model, α was increased by 50% compared to the value used in WRF.

Acknowledgements

This work was performed using HPC resources from GENCI–IDRIS (Grant 2022-AD010106852). This research has been supported by the Agence Nationale de la Recherche under grants 21-CE01-0007-01 (ASTuS) and 21-CE01-0016-01 (TuRTLES).

Data availability statement

CALIOP data v3.41 are available at https://doi.org/10.5067/CALIOP/CALIPSO/CAL_LID_L1-VALSTAGE1-V3-41 (NASA/LARC/SD/ASDC, 2016). GPS-RO data are available at the COSMIC Data Analysis and Archive centre (CDAAC) website https://cdaac-www.cosmic.ucar.edu/ .

references

Andrews, D., Holton, J., and Leovy, C.: Middle Atmosphere Dynamics., Academic Press, 1987.

Aubert, O., Bars, M. L., Gal, P. L., and Marcus, P. S.: The Universal Aspect Ratio of Vortices in Rotating Stratified Flows: Experiments and Observations, Journal of Fluid Mechanics, 706, 34–45, URL https://doi.org/10.1017/jfm.2012.176, 2012.

Baines, P. G. and Sparks, R. S. J.: Dynamics of Giant Volcanic Ash Clouds from Supervolcanic Eruptions, Geophysical Research Letters, 32, URL https://doi.org/10.1029/2005GL024597, 2005.

Berrisford, P., Marshall, J. C., and White, A. A.: Quasigeostrophic Potential Vorticity Equation in Isentropic Coordinates, J. Atmos. Sci., 50, 778–782, 1990.

Boers, R., de Laat, A. T., Zweers, D. C. S., and Dirksen, R. J.: Lifting Potential of Solar-Heated Aerosol Layers, Geophys. Res. Lett., 37, URL https://doi.org/10.1029/2010GL045171, 2010.

Brewer, A. W.: Evidence for a World Circulation Provided by the Measurements of Helium and Water Vapour Distribution in the Stratosphere, Quarterly Journal of the Royal Meteorological Society, 75, 351–363, URL https://doi.org/10.1002/qj.49707532603, 1949.

Brown, F., Marshall, L., Haynes, P. H., Garcia, R. R., Birner, T., and Schmidt, A.: On the magnitude and sensitivity of the quasi-biennial oscillation response to a tropical volcanic eruption, Atmospheric Chemistry and Physics, 23, 5335–5353, https://doi.org/10.5194/acp-23-5335-2023, 2023.

Bui, H., Yoden, S., and Nishimoto, E.: QBO-like oscillation in a three-dimensional minimal model framework of the stratosphere–troposphere coupled system, SOLA, 15, 62–67, 2019.

Butchart, N.: The Brewer-Dobson Circulation, Reviews of Geophysics, 52, 157–184, URL https://doi.org/10.1002/2013RG000448, 2014.

Cai, Z., Griessbach, S., and Hoffmann, L.: Improved Estimation of Volcanic SO_2 Injections from Satellite Retrievals and Lagrangian Transport Simulations: The 2019 Raikoke Eruption, Atmospheric Chemistry and Physics, 22, 6787–6809, URL https://doi.org/10.5194/acp-22-6787-2022, 2022.

Carr, J. L., Horváth, Á., Wu, D. L., and Friberg, M. D.: Stereo Plume Height and Motion Retrievals for the Record-Setting Hunga Tonga-Hunga Ha'apai Eruption of 15 January 2022, Geophysical Research Letters, 49, e2022GL098 131, URL https://doi.org/10.1029/2022GL098131, 2022.

Chouza, F., Leblanc, T., Barnes, J., Brewer, M., Wang, P., and Koon, D.: Long-Term (1999–2019) Variability of Stratospheric Aerosol over Mauna Loa, Hawaii, as Seen by Two Co-Located Lidars and Satellite Measurements, Atmospheric Chemistry and Physics, 20, 6821–6839, URL https://doi.org/10.5194/acp-20-6821-2020, 2020.

Cole, J. D.: On a quasi-linear parabolic equation occurring in aerodynamics, Quarterly of Applied Mathematics, 9, 225–236, URL https://doi.org/10.1090/qam/42889, 1951.

de Laat, A. T. J., Stein Zweers, D. C., Boers, R., and Tuinder, O. N. E.: A Solar Escalator: Observational Evidence of the Self-Lifting of Smoke and Aerosols by Absorption of Solar Radiation in the February 2009 Australian Black Saturday Plume, Journal of Geophysical Research: Atmospheres, 117, URL https://doi.org/10.1029/2011JD017016, 2012.

Doglioni, G., Aquila, V., Das, S., Colarco, P. R., and Zardi, D.: Dynamical Perturbation of the Stratosphere by a Pyrocumulonimbus Injection of Carbonaceous Aerosols, Atmospheric Chemistry and Physics, 22, 11 049–11 064, URL https://doi.org/10.5194/acp-22-11049-2022, 2022.

Dritschel, D. G.: Vortex Merger in Rotating Stratified Flows, Journal of Fluid Mechanics, 455, 83–101, URL https://doi.org/10.1017/S0022112001007364, 2002.

Eliassen, A.: Slow thermally or frictionally controlled meridional circulation in a circular Vortex, Astrophys. Norv., 5, 60pp, 1952.

Ertel, H.: Ein neuer hydrodynamischer Erhaltungssatz, Die Naturwissenschaften, 30, 543–544, URL https://doi.org/10.1007/BF01475602, 1942.

Foussard, A., Lapeyre, G., and Plougonven, R.: Storm track response to oceanic eddies in idealized atmospheric simulations, Journal of Climate, 32, 445–463, 2019.

Fromm, M., Lindsey, D. T., Servranckx, R., Yue, G., Trickl, T., Sica, R., Doucet, P., and Godin-Beekmann, S.: The Untold Story of Pyrocumulonimbus, Bulletin of the American Meteorological Society, 91, 1193–1210, URL https://doi.org/10.1175/2010BAMS3004.1, 2010.

Garny, H. and Randel, W. J.: Dynamic Variability of the Asian Monsoon Anticyclone Observed in Potential Vorticity and Correlations with Tracer Distributions, Journal of Geophysical Research: Atmospheres, 118, 13,421–13,433, URL https://doi.org/10.1002/2013JD020908, 2013.

Getzewich, B. J., Vaughan, M. A., Hunt, W. H., Avery, M. A., Powell, K. A., Tackett, J. L., Winker, D. M., Kar, J., Lee, K.-P., and Toth, T. D.: CALIPSO lidar calibration at 532 nm: version 4 daytime algorithm, Atmospheric Measurement Techniques, 11, 6309–6326, URL https://doi.org/10.5194/amt-11-6309-2018, 2018.

Gill, A. E.: Homogeneous Intrusions in a Rotating Stratified Fluid, Journal of Fluid Mechanics, 103, 275, URL https://doi.org/10.1017/S0022112081001341, 1981.

Glaze, L. S., Baloga, S. M., and Wilson, L.: Transport of atmospheric water vapor by volcanic eruption columns, Journal of Geophysical Research: Atmospheres, 102, 6099–6108, URL https://doi.org/10.1029/96JD03125, 1997.

Griffiths, R. W. and Linden, P. F.: The Stability of Vortices in a Rotating, Stratified Fluid, Journal of Fluid Mechanics, 105, 283–316, URL https://doi.org/10.1017/S0022112081003212, 1981.

Hassanzadeh, P., Marcus, P. S., and Gal, P. L.: The Universal Aspect Ratio of Vortices in Rotating Stratified Flows: Theory and Simulation, Journal of Fluid Mechanics, 706, 46–57, URL https://doi.org/10.1017/jfm.2012.180, 2012.

Haynes, P. H. and McIntyre, M. E.: On the Evolution of Vorticity and Potential Vorticity in the Presence of Diabatic Heating and Frictional or Other Forces, Journal of the Atmospheric Sciences, 44, 828–841, URL https://doi.org/10.1175/1520-0469(1987)044<0828:OTEOVA>2.0.CO;2, 1987.

Hersbach, H., Bell, B., Berrisford, P., Hirahara, S., Horányi, A., Muñoz-Sabater, J., Nicolas, J., Peubey, C., Radu, R., Schepers, D., Simmons, A., Soci, C., Abdalla, S., Abellan, X., Balsamo, G., Bechtold, P., Biavati, G., Bidlot, J., Bonavita, M., Chiara, G. D., Dahlgren, P., Dee, D., Diamantakis, M., Dragani, R., Flemming, J., Forbes, R., Fuentes, M., Geer, A., Haimberger, L., Healy, S., Hogan, R. J., Hólm, E., Janisková, M., Keeley, S., Laloyaux, P., Lopez, P., Lupu, C., Radnoti, G., Rosnay, P. d., Rozum, I., Vamborg, F., Villaume, S., and Thépaut, J.-N.: The ERA5 global reanalysis, Quarterly Journal of the Royal Meteorological Society, 146, 1999–2049, URL https://doi.org/10.1002/qj.3803, 2020.

Holasek, R. E., Self, S., and Woods, A. W.: Satellite Observations and Interpretation of the 1991 Mount Pinatubo Eruption Plumes, Journal of Geophysical Research: Solid Earth, 101, 27 635–27 655, URL https://doi.org/10.1029/96JB01179, 1996.

Hopf, E.: The partial differential equation ut + uux = μxx, Communications on Pure and Applied Mathematics, 3, 201–230, URL https://doi.org/10.1002/cpa.3160030302, 1950.

Hoskins, B., Pedder, M., and Jones, D. W.: The Omega Equation and Potential Vorticity, Quarterly Journal of the Royal Meteorological Society, 129, 3277–3303, URL https://doi.org/10.1256/qj.02.135, 2003.

Hoskins, B. J., McIntyre, M. E., and Robertson, A. W.: On the Use and Significance of Isentropic Potential Vorticity Maps, Quarterly Journal of the Royal Meteorological Society, 111, 877–946, URL https://doi.org/10.1002/qj.49711147002, 1985.

Kablick, G. P., Allen, D. R., Fromm, M. D., and Nedoluha, G. E.: Australian PyroCb Smoke Generates Synoptic-Scale Stratospheric Anticyclones, Geophysical Research Letters, 47, URL https://doi.org/10.1029/2020GL088101, 2020.

Kar, J., Vaughan, M. A., Lee, K.-P., Tackett, J. L., Avery, M. A., Garnier, A., Getzewich, B. J., Hunt, W. H., Josset, D., Liu, Z., Lucker, P. L., Magill, B., Omar, A. H., Pelon, J., Rogers, R. R., Toth, T. D., Trepte, C. R., Vernier, J.-P., Winker, D. M., and Young, S. A.: CALIPSO Lidar Calibration at 532 nm: Version 4 Nighttime Algorithm, Atmospheric Measurement Techniques, 11, 1459–1479, URL https://doi.org/10.5194/amt-11-1459-2018, 2018.

Khaykin, S., Legras, B., Bucci, S., Sellitto, P., Isaksen, L., Tencé, F., Bekki, S., Bourassa, A., Rieger, L., Zawada, D., Jumelet, J., and Godin-Beekmann, S.: The 2019/20 Australian Wildfires Generated a Persistent Smoke-Charged Vortex Rising up to 35 Km Altitude, Communications Earth & Environment, 1, 22, URL https://doi.org/10.1038/s43247-020-00022-5, 2020.

Khaykin, S., Podglajen, A., Ploeger, F., Grooß, J.-U., Tence, F., Bekki, S., Khlopenkov, K., Bedka, K., Rieger, L., Baron, A., Godin-Beekmann, S., Legras, B., Sellitto, P., Sakai, T., Barnes, J., Uchino, O., Morino, I., Nagai, T., Wing, R., Baumgarten, G., Gerding, M., Duflot, V., Payen, G., Jumelet, J., Querel, R., Liley, B., Bourassa, A., Clouser, B., Feofilov, A., Hauchecorne, A., and Ravetta, F.: Global Perturbation of Stratospheric Water and Aerosol Burden by Hunga Eruption, Communications Earth & Environment, 3, 1–15, URL https://doi.org/10.1038/s43247-022-00652-x, 2022a.

Khaykin, S. M., Godin-Beekmann, S., Hauchecorne, A., Pelon, J., Ravetta, F., and Keckhut, P.: Stratospheric Smoke With Unprecedentedly High Backscatter Observed by Lidars Above Southern France, Geophysical Research Letters, 45, 1639–1646, URL https://doi.org/10.1002/2017GL076763, 2018.

Khaykin, S. M., de Laat, A. T. J., Godin-Beekmann, S., Hauchecorne, A., and Ratynski, M.: Unexpected Self-Lofting and Dynamical Confinement of Volcanic Plumes: The Raikoke 2019 Case, Scientific Reports, 12, 22 409, URL https://doi.org/10.1038/s41598-022-27021-0, 2022b.

Legras, B., Duchamp, C., Sellitto, P., Podglajen, A., Carboni, E., Siddans, R., Grooß, J.-U., Khaykin, S., and Ploeger, F.: The Evolution and Dynamics of the Hunga Tonga–Hunga Ha'apai Sulfate Aerosol Plume in the Stratosphere, Atmospheric Chemistry and Physics, 22, 14 957–14 970, URL https://doi.org/10.5194/acp-22-14957-2022, 2022.

Lestrelin, H., Legras, B., Podglajen, A., and Salihoglu, M.: Smoke-Charged Vortices in the Stratosphere Generated by Wildfires and Their Behaviour in Both Hemispheres: Comparing Australia 2020 to Canada 2017, Atmospheric Chemistry and Physics, 21, 7113–7134, URL https://doi.org/10.5194/acp-21-7113-2021, 2021.

Millán, L., Santee, M. L., Lambert, A., Livesey, N. J., Werner, F., Schwartz, M. J., Pumphrey, H. C., Manney, G. L., Wang, Y., Su, H., Wu, L., Read, W. G., and Froidevaux, L.: The Hunga Tonga-Hunga Ha'apai Hydration of the Stratosphere, Geophysical Research Letters, 49, e2022GL099 381, URL https://doi.org/10.1029/2022GL099381, 2022.

Ohneiser, K., Ansmann, A., Baars, H., Seifert, P., Barja, B., Jimenez, C., Radenz, M., Teisseire, A., Floutsi, A., Haarig, M., Foth, A., Chudnovsky, A., Engelmann, R., Zamorano, F., Bühl, J., and Wandinger, U.: Smoke of Extreme Australian Bushfires Observed in the Stratosphere over Punta Arenas, Chile, in January 2020: Optical Thickness, Lidar Ratios, and Depolarization Ratios at 355 and 532 nm, Atmospheric Chemistry and Physics, 20, 8003–8015, URL https://doi.org/10.5194/acp-20-8003-2020, 2020.

Peterson, D. A., Fromm, M. D., McRae, R. H. D., Campbell, J. R., Hyer, E. J., Taha, G., Camacho, C. P., Kablick, G. P., Schmidt, C. C., and DeLand, M. T.: Australia's Black Summer Pyrocumulonimbus Super Outbreak Reveals Potential for Increasingly Extreme Stratospheric Smoke Events, npj Clim Atmos Sci, 4, 38, URL https://doi.org/10.1038/s41612-021-00192-9, 2021.

Proud, S. R., Prata, A. T., and Schmauß, S.: The January 2022 Eruption of Hunga Tonga-Hunga Ha'apai Volcano Reached the Mesosphere, Science, 378, 554–557, URL https://doi.org/10.1126/science.abo4076, 2022.

Pumphrey, H. C., Schwartz, M. J., Santee, M. L., Kablick III, G. P., Fromm, M. D., and Livesey, N. J.: Microwave Limb Sounder (MLS) Observations of Biomass Burning Products in the Stratosphere from Canadian Forest Fires in August 2017, Atmospheric Chemistry and Physics, 21, 16 645–16 659, URL https://doi.org/10.5194/acp-21-16645-2021, 2021.

Reinaud, J. N. and Dritschel, D. G.: The Merger of Vertically Offset Quasi-Geostrophic Vortices, Journal of Fluid Mechanics, 469, 287–315, URL https://doi.org/10.1017/S0022112002001854, 2002.

Schallock, J., Brühl, C., Bingen, C., Höpfner, M., Rieger, L., and Lelieveld, J.: Reconstructing volcanic radiative forcing since 1990, using a comprehensive emission inventory and spatially resolved sulfur injections from satellite data in a chemistry-climate model, Atmospheric Chemistry and Physics, 23, 1169–1207, https://doi.org/https://doi.org/10.5194/acp-23-1169-2023, 2023.

Schoeberl, M. R., Lait, L. R., Newman, P. A., and Rosenfield, J. E.: The structure of the polar vortex, Journal of Geophysical Research, 97, 7859, https://doi.org/https://doi.org/10.1029/91JD02168, 1992.

Schoeberl, M. R., Wang, Y., Ueyama, R., Taha, G., and Yu, W.: The Cross Equatorial Transport of the Hunga Tonga-Hunga Ha'apai Eruption Plume, Geophysical Research Letters, 50, e2022GL102 443, URL https://doi.org/10.1029/2022GL102443, 2023.

Schubert, W. H.: Bernhard Haurwitz Memorial Lecture (2017): Potential Vorticity Aspects of Tropical Dynamics, 2018.

Schubert, W. H. and Alworth, B. T.: Evolution of Potential Vorticity in Tropical Cyclones, Quarterly Journal of the Royal Meteorological Society, 113, 147–162, URL https://doi.org/10.1002/qj.49711347509, 1987.

Schubert, W. H. and Hack, J. J.: Transformed Eliassen Balanced Vortex Model, Journal of the Atmospheric Sciences, 40, 1571–1583, URL https://doi.org/10.1175/1520-0469(1983)040<1571:TEBVM>2.0.CO;2, 1983.

Sellitto, P., Podglajen, A., Belhadji, R., Boichu, M., Carboni, E., Cuesta, J., Duchamp, C., Kloss, C., Siddans, R., Bègue, N., Blarel, L., Jegou, F., Khaykin, S., Renard, J.-B., and Legras, B.: The Unexpected Radiative Impact of the Hunga Tonga Eruption of 15th January 2022, Communications Earth & Environment, 3, 1–10, URL https://doi.org/10.1038/s43247-022-00618-z, 2022.

Sellitto, P., Belhadji, R., Cuesta, J., Podglajen, A., and Legras, B.: Radiative impacts of the Australian bushfires 2019–2020 – Part 2: Large-scale and in-vortex radiative heating, EGUsphere, 2023, 1–19, https://doi.org/10.5194/egusphere-2023-1067, 2023.

Shutts, G.: Some Exact Solutions to the Semi-Geostrophic Equations for Uniform Potential Vorticity Flows, Geophysical & Astrophysical Fluid Dynamics, 57, 99–114, URL https://doi.org/10.1080/03091929108225230, 1991.

Shutts, G. J. and Thorpe, A. J.: Some Aspects of Vortices in Rotating Stratified Fluids, Pure and Applied Geophysics, 116, 993–1006, URL https://doi.org/10.1007/BF00874667, 1978.

Shutts, G. J., Booth, M., and Norbury, J.: A Geometric Model of Balanced, Axisymmetric Flows with Embedded Penetrative Convection, Journal of the Atmospheric Sciences, 45, 2609–2621, 1988.

Skamarock, C., Klemp, B., Dudhia, J., Gill, O., Barker, D., Duda, G., Huang, X.-y., Wang, W., and Powers, G.: A Description of the Advanced Research WRF Version 3, URL https://doi.org/10.5065/D68S4MVH, 2008.

Smagorinski, J.: GENERAL CIRCULATION EXPERIMENTS WITH THE PRIMITIVE EQUATIONS: I. THE BASIC EXPERIMENT, Monthly Weather Review, 91, 99 – 164, https://doi.org/https://doi.org/10.1175/1520-0493(1963)091<0099:GCEWTP>2.3.CO;2, 1963.

Thorpe, A. J.: Diagnosis of Balanced Vortex Structure Using Potential Vorticity, Journal of the Atmospheric Sciences, 42, 397–406, URL https://doi.org/10.1175/1520-0469(1985)042<0397:DOBVSU>2.0.CO;2, 1985.

Vaughan, M. A., Young, S. A., Winker, D. M., Powell, K. A., Omar, A. H., Liu, Z., Hu, Y., and Hostetler, C. A.: Fully automated analysis of space-based lidar data: an overview of the CALIPSO retrieval algorithms and data products, Proc. SPIE 5575, Laser Radar Techniques for Atmospheric Sensing, (4 November 2004), URL https://doi.org/10.1117/12.572024, 2004.

Whitham, G. B.: Burgers' Equation, chap. 4, pp. 96–112, John Wiley & Sons, Ltd, https://doi.org/https://doi.org/10.1002/9781118032954.ch4, 1999.

Winker, D. M., Pelon, J., Jr, J. A. C., Ackerman, S. A., Charlson, R. J., Colarco, P. R., Flamant, P., Fu, Q., Hoff, R. M., Kittaka, C., Kubar, T. L., Treut, H. L., Mccormick, M. P., Mégie, G., Poole, L., Powell, K., Trepte, C., Vaughan, M. A., and Wielicki, B. A.: The CALIPSO mission: A Global 3D View of Aerosols and Clouds, Bulletin of the American Meteorological Society, 91, 1211–1230, 2010.

Yu, P., Toon, O. B., Bardeen, C. G., Zhu, Y., Rosenlof, K. H., Portmann, R. W., Thornberry, T. D., Gao, R.-S., Davis, S. M., Wolf, E. T., de Gouw, J., Peterson, D. A., Fromm, M. D., and Robock, A.: Black carbon lofts wildfire smoke high into the stratosphere to form a persistent plume, Science, 365, 587–590, URL https://doi.org/10.1126/science.aax1748, 2019.

GRAPHICAL ABSTRACT

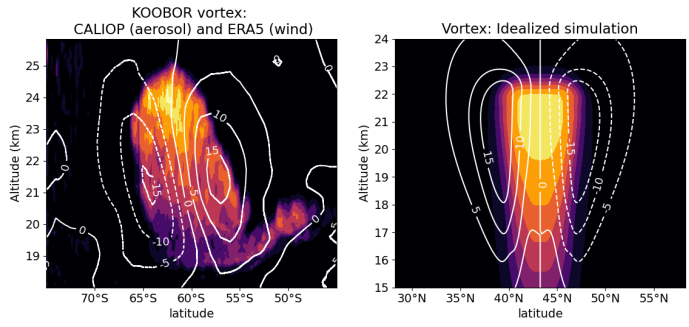

Satellite and reanalysis data have revealed the organization of stratospheric plumes from extreme wildfires and volcanic eruptions into synoptic-scale anticyclones. Previous research recognised the role of radiative heating from sunlight-absorbing aerosols in this phenomenon. Here, a reduced model is introduced which attributes the structures to diabatic forcing by a Lagrangian tracer. By investigating the forced flow using potential vorticity theory and comparing analytical results to numerical simulations, the study offers the first comprehensive understanding of this atmospheric occurrence.